Drift kinetic theory of the NTM magnetic islands in a finite beta general geometry tokamak plasma

Drift kinetic theory of the NTM magnetic islands in a finite beta general geometry tokamak plasma

A.V. Dudkovskaia[1,*] , **L. Bardoczi**[2] , **J.W. Connor**[3] , **D. Dickinson**[1] , **P. Hill**[1] ,
K. Imada[1] , **S. Leigh**[1] , **N. Richner**[4] , **T. Shi**[5] and **H.R. Wilson**[1]

[1] York Plasma Institute, Department of Physics, University of York, Heslington, York YO10 5DD, United Kingdom of Great Britain and Northern Ireland
[2] General Atomics, PO Box 85608, San Diego, CA 92186-5608, United States of America
[3] UKAEA-CCFE, Culham Science Centre, Abingdon Oxon OX14 3DB, United Kingdom of Great Britain and Northern Ireland
[4] Oak Ridge Associated Universities, Oak Ridge, TN 37831, United States of America
[5] Institute of Plasma Physics, Chinese Academy of Sciences, Hefei 230031, China

E-mail: alexandra.dudkovskaia@york.ac.uk

CrossMark

Abstract

In (Imada *et al* 2019 *Nucl. Fusion* **59** 046016 and references therein) a new 4D drift kinetic nonlinear theory, valid in the limit of a low beta, small inverse aspect ratio, circular cross section, toroidal geometry, to describe the plasma response to the neoclassical tearing mode (NTM) magnetic perturbation is derived. In (Dudkovskaia *et al* 2021 *Plasma Phys. Control. Fusion* **63** 054001) this theory is reduced in a low collisionality limit, which allows a dimensionality reduction to a 3D problem to efficiently resolve the collisional dissipation layer in the vicinity of the trapped-passing boundary. (Dudkovskaia *et al* 2021 *Plasma Phys. Control. Fusion* **63** 054001) adopts an improved model for the magnetic drift frequency, which reduces *the threshold magnetic island half-width* from $8.73\rho_{bi}$, where ρ_{bi} is the trapped ion banana orbit width, to $1.46\rho_{bi}$, making it in closer agreement with experimental observations for the large aspect ratio tokamak equilibrium. In the present paper, the theory is extended to a high beta, arbitrary tokamak geometry to capture the plasma shaping effects on the NTM threshold physics with the focus on the non-zero triangularity discharges that are known to have a strong impact on the plasma MHD stability. First, it is found that the higher triangularity plasma is more prone to NTMs which is in agreement with the 2/1 tearing mode onset relative frequency measurements in DIII-D. Second, the NTM threshold dependence on the tokamak inverse aspect ratio obtained in (Dudkovskaia *et al* 2021 *Plasma Phys. Control. Fusion* **63** 054001) is refined and extended to a finite aspect ratio limit. Third, the NTM threshold dependence on poloidal beta is obtained and benchmarked against the EAST threshold island width measurements.

Keywords: drift kinetic theory, neoclassical tearing mode, magnetic island, tokamak plasma, bootstrap current, plasma shaping effects, plasma beta

(Some figures may appear in colour only in the online journal)

---

* Author to whom any correspondence should be addressed.

1. Introduction

Neoclassical tearing modes (NTMs) are amongst the main performance limiting, resistive magnetohydrodynamic (MHD) plasma instabilities in a tokamak. Their presence is anticipated for the ITER baseline scenario, such as ELMy H-mode [1], as well as in advanced tokamak scenarios, e.g. as planned for JT-60SA. NTMs arise from filamentation of the current density, which modifies the equilibrium magnetic field topology, forming magnetic islands. The main drive for NTMs is provided by helical holes in the bootstrap current density that arise as a result of the pressure profile flattening across the island [2, 3]. This conventional theory is correct provided there are no heat or particle sources/sinks within the island and the island width is sufficiently large, i.e. much larger than the trapped ion banana orbit width. NTM stabilisation can be achieved by current drive. For example, on ITER it is planned to control NTMs by launching microwaves at the electron cyclotron frequency to restore the missing bootstrap current inside the island. This control scheme is highly sensitive to the radial localisation of current drive. A key parameter for quantifying the NTM control system (i.e. the amount of power required to stabilise the mode and how localised it has to be) is the *magnetic island threshold half-width*, w_c, below which magnetic islands are observed experimentally to self-heal. The knowledge of w_c will help to optimise control schemes [4] on present devices and extrapolate requirements on current drive to ITER and DEMO.

Along with the bootstrap drive, Δ_{bs}, there are three other main contributions to the perturbed current density parallel to the magnetic field lines, and hence to island evolution. These are (a) the inductive contribution associated with the island growth, proportional to dw/dt, where w is the magnetic island half-width, (b) the polarisation contribution, Δ_{pol}, and (c) curvature effects, Δ_{cur}. These are localised in the vicinity of the magnetic island, and cause a jump in the perturbed magnetic flux gradient across the associated resonant surface. This jump must be matched to the parameter Δ' derived from the global equilibrium properties using ideal MHD [5]. The polarisation current, and hence Δ_{pol}, is highly sensitive to the physics of the boundary layer that surrounds the island separatrix and plays a role for islands of width comparable to ρ_{bi}. In the present paper we set the equilibrium radial electric field to zero in the island rest frame. This then removes the polarisation contribution associated with the equilibrium electric field from the analysis. Any polarisation current contribution then arises from the self-consistent, localised electrostatic potential, required for quasi-neutrality.

The NTM drive provided by the perturbed bootstrap current exists in a low collisionality tokamak regime and is proportional to a linear combination of the ion/electron density/temperature gradients. The theory of this bootstrap drive is well-developed in the limit of large islands [6–8] and [9] (for $w \gg \rho_{bi}$ but allowing $w \sim \rho_{\vartheta i} = \varepsilon^{-1/2}\rho_{bi}$, where $\rho_{\vartheta i}$ is the ion poloidal Larmor radius and $\varepsilon = r_s/R_0$ is the tokamak inverse aspect ratio with r_s denoting the rational surface location and R_0 being the tokamak major radius). There are a few theories that have attempted to consider small islands in the vicinity of

the NTM threshold. For example, [10] addresses the heat transport model. For large islands, the pressure gradient removal in the vicinity of the island O-point is the result of the dominant parallel transport. [10] retains the perpendicular transport and estimates the threshold island width by balancing it against the parallel transport. The calculation is carried out in the collisional limit of parallel transport. [11] provides a calculation similar to [10] but in the collisionless limit, employing a simplified kinetic equation and balancing the parallel streaming with radial diffusion. A rigorous treatment of magnetic islands of width comparable to the trapped ion banana orbit width requires the kinetic approach to capture the finite orbit width effects. For example, [12, 13] solves the drift kinetic equation in a low beta, circular cross section tokamak limit and confirms the ion density gradient restoration across islands of width comparable to ρ_{bi}; however, it does not provide an accurate solution for the electron component, being inconsistent with plasma quasi-neutrality. [14, 15] extends the model to gyrokinetics and allows for the electrostatic potential to be determined self-consistently from the electron response, however, not fully capturing the neoclassical physics and neglecting collisions.

In [16–19] we have developed a new self-consistent drift kinetic theory and associated drift island formalism to describe how plasma responds to the NTM magnetic perturbation. To implement this, two numerical codes have been developed: 4D DK- [18] and 3D RDK-NTM [19] (the 3D version, developed in [19], averages the distribution function over streamlines to reduce the 4D version and is valid for small, ITER-relevant collisions). They both assume a low beta large aspect ratio tokamak and consider the limit of small islands, comparable to ρ_{bi}, to retain the effects of finite orbit widths relevant for the NTM threshold island width. [19] considers how the parallel current density varies as the magnetic island width approaches the ion poloidal Larmor radius. For large islands of half-width $w \gg \rho_{\vartheta i}$, no parallel current is supported inside the magnetic island, providing a strong drive for NTMs, in agreement with the conventional theory of large magnetic islands. As the island width decreases towards values comparable to $\rho_{\vartheta i}$, we find significant stabilising currents in the vicinity of the magnetic island separatrix close to X-points that spread into the island region, as well as growing destabilising currents just outside the separatrix. Their balance determines the threshold island width that is found numerically to be a few ion banana widths for a chosen equilibrium scenario, qualitatively matching data from DIII-D, ASDEX-U and JT-60U. Although the threshold scaling with the inverse aspect ratio as $\varepsilon^{1/2}$, recovered in [19], indicates a role for trapped particles, the theory shows that the threshold mechanism originates from the drift orbits associated with passing particles. Specifically, passing particles are shown to follow 'drift islands' which are of the same shape as the magnetic island, but shifted radially relative to it by a few $\rho_{\vartheta i}$. The passing particle distribution function is then found to be flattened across these drift islands and, for $w \sim \rho_{\vartheta i}$, maintains a density gradient across the magnetic island.

To provide a quantitative prediction to compare with experiment, in the present paper we extend the drift island formalism

[18, 19] to a finite beta, arbitrary tokamak geometry plasma configuration. This then captures the plasma curvature effects on the NTM threshold physics. The effects of the plasma shaping are expected to be less significant in conventional tokamaks, based on a number of predictions [20, 21]; however, if stabilising, they can enhance the passing particle drift mechanism for the threshold discovered in [19]. Furthermore, they are likely to be particularly important for spherical tokamaks.

The paper is organised as follows. In section 2 we define the coordinate system. In section 3 we introduce a general kinetic equation that we gyro-average in section 4 to obtain the drift kinetic equation extended to a finite beta limit. In section 5 we define the perturbed magnetic field topology associated with the magnetic island and proceed to calculating the plasma response to the magnetic field perturbation in section 6. This is followed by conclusions in section 7.

2. Coordinate system

We define an orthogonal coordinate system with the basis formed by the unit vectors $(\boldsymbol{b}, \boldsymbol{e}_2, \boldsymbol{e}_3)$. Note, $\boldsymbol{b} = \boldsymbol{e}_2 \times \boldsymbol{e}_3$, $\boldsymbol{e}_2 \cdot d\boldsymbol{e}_3/dt = -\boldsymbol{e}_3 \cdot d\boldsymbol{e}_2/dt$ and $\boldsymbol{e}_2 \cdot d\boldsymbol{e}_2/dt = 0$ and so on, where d/dt denotes the time derivative following the particle orbit, $\boldsymbol{x}$. The unit vector $\boldsymbol{b} = \boldsymbol{B}/B$, where $\boldsymbol{B}$ is the total magnetic field and $B = |\boldsymbol{B}|$. We write the velocity as

$$\boldsymbol{V} = \boldsymbol{u} + \boldsymbol{s} \tag{1}$$

with

$$\boldsymbol{u} = u\boldsymbol{b} \equiv V_{\parallel}\boldsymbol{b} \tag{2}$$

being the velocity component along and

$$\boldsymbol{s} \equiv \boldsymbol{V}_{\perp} = s(\boldsymbol{e}_2 \cos\alpha - \boldsymbol{e}_3 \sin\alpha) \equiv s\hat{\boldsymbol{s}} \tag{3}$$

across the magnetic field lines. Here α denotes the gyrophase angle. The Larmor radius vector is then given by

$$\boldsymbol{\rho} = \frac{\boldsymbol{b} \times \boldsymbol{s}}{\omega_c} = \rho(\boldsymbol{e}_3 \cos\alpha + \boldsymbol{e}_2 \sin\alpha) \equiv \rho\hat{\boldsymbol{\rho}}, \tag{4}$$

where $\omega_c = eZB/m$ is the cyclotron frequency, eZ and m are the particle charge and mass, respectively; $\rho = s/\omega_c$[6]. The equation of motion for these particles reads

$$m\frac{d(\boldsymbol{u} + \boldsymbol{s})}{dt} = eZ\boldsymbol{E} - m\omega_c s\hat{\boldsymbol{\rho}}, \tag{5}$$

where $eZ\boldsymbol{V} \times \boldsymbol{B} = -m\omega_c s\hat{\boldsymbol{\rho}}$ and $\boldsymbol{E} = -\boldsymbol{\nabla}\Phi - \partial\boldsymbol{A}/\partial t$ is the electric field; Φ is the electrostatic potential and $\boldsymbol{A}$ is the magnetic vector potential. We define the magnetic moment (per unit mass) as $\mu = s^2/2B$ and the total energy (per unit mass) as $U = \mu B + u^2/2 + eZ\Phi/m \equiv V^2/2 + eZ\Phi/m$, where V is the particle speed.

---

[6] The particle species index, j, is to be omitted for simplicity and is to be introduced only when it is necessary to distinguish ions and electrons.

3. General kinetic equation in $\{t, \boldsymbol{x}, U, \mu, \alpha\}$ space

The general kinetic equation for the particle distribution function, f, in $\{t, \boldsymbol{x}, U, \mu, \alpha\}$ space reads

$$\omega_c \left.\frac{\partial f}{\partial \alpha}\right|_{\boldsymbol{x}, U, \mu} + \mathcal{L}f = Cf, \tag{6}$$

where

$$\mathcal{L} = \frac{\partial}{\partial t} + \boldsymbol{V} \cdot \boldsymbol{\nabla} + \frac{d\mu}{dt} \left.\frac{\partial}{\partial \mu}\right|_{\boldsymbol{x}, U, \alpha} + \frac{dU}{dt} \left.\frac{\partial}{\partial U}\right|_{\boldsymbol{x}, \mu, \alpha}$$
$$+ \left(\frac{d\alpha}{dt} - \omega_c\right) \left.\frac{\partial}{\partial \alpha}\right|_{\boldsymbol{x}, U, \mu}. \tag{7}$$

The collision operator, C, is to be specified below. From the equation of motion, equation (5), it can be shown that

$$\frac{d\mu}{dt} = -\frac{\mu}{B}\frac{dB}{dt} - \frac{u}{B}\frac{d\boldsymbol{b}}{dt} \cdot \boldsymbol{s} + \frac{eZ}{mB}\boldsymbol{E} \cdot \boldsymbol{s}, \tag{8}$$

$$\frac{dU}{dt} = \frac{eZ}{m}\frac{\partial\Phi}{\partial t} - \frac{eZ}{m}\boldsymbol{V} \cdot \frac{\partial\boldsymbol{A}}{\partial t} \tag{9}$$

and

$$\frac{d\alpha}{dt} = \omega_c + \boldsymbol{e}_3 \cdot \frac{d\boldsymbol{e}_2}{dt} + \frac{u}{s}\frac{d\boldsymbol{b}}{dt} \cdot \hat{\boldsymbol{\rho}} - \frac{eZ}{ms}\boldsymbol{E} \cdot \hat{\boldsymbol{\rho}}. \tag{10}$$

The derivation is similar to that presented in [22].

4. Gyro-averaging. Drift kinetic equation

We introduce a small parameter:

$$\delta_* = \frac{\rho}{L} \ll 1,$$

where ρ is the particle Larmor radius. L denotes the characteristic size of the system. The particle distribution function is

$$f = f_0 + f_1 + \mathcal{O}\left(\delta_*^2 f_0\right). \tag{11}$$

Expanding equation (6) in powers of δ_* and retaining the $\mathcal{O}\left(\delta_*^1 \frac{V_t}{L} f_0\right)$ corrections (V_t is the particle thermal speed) to capture the plasma drift effects, we obtain an extended drift kinetic equation for f_0 (see appendix A for a detailed derivation):

$$\frac{\partial f_0}{\partial t} + (\boldsymbol{u} + \boldsymbol{u}_D + \boldsymbol{V}_D) \cdot \boldsymbol{\nabla}f_0 + \left.\frac{d\mu}{dt}\right|_{\text{avg}} \frac{\partial f_0}{\partial \mu} + \left\{ \mu\left[\boldsymbol{\nabla} \times \frac{\partial\boldsymbol{A}}{\partial t}\right] \cdot \boldsymbol{b} \right.$$
$$\left. + \frac{eZ}{m}\left[\frac{\partial\Phi}{\partial t} - (\boldsymbol{u} + \boldsymbol{u}_D + \boldsymbol{V}_D) \cdot \frac{\partial\boldsymbol{A}}{\partial t}\right] \right\} \frac{\partial f_0}{\partial U} = Cf_0 \tag{12}$$

in $\{t, \boldsymbol{x}, U, \mu\}$ space or

$$\frac{\partial f_0}{\partial t} + (\boldsymbol{u} + \boldsymbol{u}_D + \boldsymbol{V}_D) \cdot \boldsymbol{\nabla}f_0 + \left.\frac{d\mu}{dt}\right|_{\text{avg}} \frac{\partial f_0}{\partial \mu}$$
$$+ \left\{ \mu\left[\boldsymbol{\nabla} \times \frac{\partial\boldsymbol{A}}{\partial t}\right] \cdot \boldsymbol{b} + \frac{eZ}{m}(\boldsymbol{u} + \boldsymbol{u}_D + \boldsymbol{V}_D) \cdot \boldsymbol{E} \right\} \frac{\partial f_0}{V\partial V} = Cf_0 \tag{13}$$

in $\{t, \boldsymbol{x}, V, \mu\}$ space. Here the parallel drift velocity is

$$\boldsymbol{u}_D = \frac{s^2}{2\omega_c} \frac{\mu_0 j_\parallel}{B} \boldsymbol{b} \tag{14}$$

with $\mu_0 j_\parallel / B$ being provided by equation (A.12). $\boldsymbol{V}_D$ is the drift velocity defined as $\boldsymbol{V}_D = \boldsymbol{V}_E + \boldsymbol{V}_d$ with

$$\boldsymbol{V}_E = \frac{\boldsymbol{E} \times \boldsymbol{b}}{B}, \quad \boldsymbol{V}_d = \frac{1}{\omega_c} \boldsymbol{b} \times \left[\frac{s^2}{2} \boldsymbol{\nabla} \ln B + u^2 (\boldsymbol{b} \cdot \boldsymbol{\nabla}) \boldsymbol{b} \right], \tag{15}$$

and

$$\frac{1}{\mu} \frac{d\mu}{dt} \bigg|_{\text{avg}} = u(\boldsymbol{b} \cdot \boldsymbol{\nabla}) \left(\frac{u}{\omega_c} \frac{\mu_0 j_\parallel}{B} \right) + \frac{s^2}{\omega_c} \frac{\mu_0}{B} (\boldsymbol{j}_\perp \cdot \boldsymbol{\nabla} \ln B)$$
$$+ \frac{2}{B} [\boldsymbol{b} \times (\boldsymbol{b} \cdot \boldsymbol{\nabla}) \boldsymbol{b}] \cdot \frac{\partial \boldsymbol{A}}{\partial t} - \frac{2u}{\omega_c} \left[\boldsymbol{b} \times \frac{\partial \boldsymbol{b}}{\partial t} \right] \cdot (\boldsymbol{b} \cdot \boldsymbol{\nabla}) \boldsymbol{b}. \tag{16}$$

The $\frac{d\mu}{dt}\big|_{\text{avg}}$ term (see appendix B for a detailed derivation) is usually ordered out from the drift kinetic equation, being considered as the $\mathcal{O}\left(\beta \delta_* \frac{V_t}{L} f_0\right)$ correction, where β is the ratio of plasma pressure, p, to the magnetic field pressure, $B^2/(2\mu_0)$. However, to allow the finite beta limit, we must retain the magnetic moment variation of the distribution function in the Vlasov operator.

Equation (13) with equations (14)–(16) form the drift kinetic equation to be employed to describe the plasma response to the NTM magnetic island in a finite beta arbitrary tokamak geometry plasma.

5. Magnetic topology

We consider a finite beta axisymmetric tokamak plasma with equilibrium magnetic field given by

$$\boldsymbol{B}_0 = I(\psi) \boldsymbol{\nabla} \varphi + \boldsymbol{\nabla} \varphi \times \boldsymbol{\nabla} \psi, \tag{17}$$

where $I = RB_\varphi$ depends on poloidal current, R is the varying tokamak major radius and B_φ is the toroidal component of the magnetic field. Here ψ is the poloidal flux function introduced to label nested magnetic flux surfaces, and φ denotes the toroidal angle. The magnetic field perturbation associated with a single isolated magnetic island is

$$\boldsymbol{B}_1 = \boldsymbol{\nabla} \times (A_\parallel^1 \boldsymbol{b}_0) + \boldsymbol{\nabla} \times \boldsymbol{A}_\perp^1 \tag{18}$$

with

$$A_\parallel^1 = -\frac{\tilde{\psi}}{R} \cos(\mathrm{n}\xi), \tag{19}$$

where $\tilde{\psi} = (w_\psi{}^2/4)(q'/q)$ and w_ψ being the island half-width in ψ space related to w in r space via $w = w_\psi/(RB_\vartheta)$, and $\boldsymbol{b}_0 = \boldsymbol{B}_0/|\boldsymbol{B}_0|$ is the unit vector along the equilibrium magnetic field lines[7]. $\boldsymbol{A}_\perp^1$ is the perpendicular component of the

---

[7] For equilibrium quantities, i.e. in the absence of the magnetic island, prime denotes the derivative with respect to ψ.

perturbed vector potential. B_ϑ is the poloidal component of the magnetic field. Here we have defined the helical angle as $\xi = \varphi - q_s \vartheta$ with $q_s = \mathrm{m/n}$ being the safety factor, q, evaluated at the rational surface, i.e. the ratio of the poloidal m to the toroidal n mode number; ϑ is the poloidal angle with $\boldsymbol{\nabla}\psi \cdot \boldsymbol{\nabla}\vartheta = \vartheta' R^2 B_\vartheta^2$. It can be shown that

$$\boldsymbol{B}_1 \cdot \boldsymbol{\nabla} p_\varphi = -\frac{\mathrm{n}\tilde{\psi}}{RB_0} B_\vartheta^2 \left(1 + \frac{q_s}{q} \frac{B_\varphi^2}{B_\vartheta^2} \right) \sin(\mathrm{n}\xi)$$
$$+ \frac{\tilde{\psi}}{R^2 B_0^2} \frac{I^2}{qR^2} \frac{\partial(RB_0)}{\partial\vartheta} \bigg|_{\psi,\varphi} \cos(\mathrm{n}\xi) + \mathcal{O}\left(\delta_* \Delta^2 L B_0^2\right), \tag{20}$$

where $p_\varphi = \psi - \psi_s - Iu/\omega_c$ and ψ_s represents the position of the rational surface in ψ space. Here we have introduced the second small parameter:

$$\Delta = \frac{w}{a} \ll 1, \tag{21}$$

where a is the tokamak minor radius. The $\mathcal{O}\left(\delta_* \Delta^2 L B_0^2\right)$ terms in equation (20) provide $\mathcal{O}\left(\delta_* \Delta^2 \frac{V_t}{L} f_0\right)$ corrections in the drift kinetic equation and thus will be omitted. The perturbed distribution function associated with the magnetic island perturbation is assumed to be $\sim \Delta f_0$. Then from Ampère's law, $|\boldsymbol{B}_1| \sim \Delta^2 B_0$ with $\boldsymbol{\nabla} \times (B_\parallel^1 \boldsymbol{b}_0) \sim \boldsymbol{\nabla}_\perp B_\parallel^1 \times \boldsymbol{b}_0$ and $B_\parallel^1 \equiv (\boldsymbol{B}_1 \cdot \boldsymbol{b}_0) \sim \beta \Delta^2 B_0$, provided $|\boldsymbol{\nabla}_\perp| \sim 1/w$ when acting on perturbed quantities. Since

$$B_\parallel^1 (\boldsymbol{b}_0 \cdot \boldsymbol{\nabla} p_\varphi) = -B_\parallel^1 \frac{\partial}{\partial\vartheta} \bigg|_{\psi,\varphi} \left(\frac{Iu}{\omega_c} \right) \frac{I}{qR^2 B_0} \sim \beta \delta_* \Delta^2 L B_0^2,$$

the second term in equation (18) results in the $\mathcal{O}\left(\delta_* \Delta^2 \frac{V_t}{L} f_0\right)$ corrections in the drift kinetic equation. Note, the radial variation of equilibrium quantities, including q and q', results in the $\mathcal{O}\left(\delta_* \Delta^2 L B_0^2\right)$ corrections in equation (20).

5.1. Note on drift kinetic ordering in the NTM description

According to experiment [23, 24], the threshold width is about $(2-3)\rho_{bi}$. Therefore, the island widths we are interested in are $w \sim \rho_{bi} \sim \varepsilon^{1/2} \rho_{\vartheta i}$, where $\rho_{\vartheta i}$ is the ion poloidal Larmor radius related to the ion Larmor radius via $\rho_{\vartheta i} = \rho_i/\Theta$ with $\Theta = B_\vartheta/B_0$. To eliminate the gyro-angle dependence in the drift kinetic theory, we expand the particle distribution function in powers of δ_* and perform averaging over α at fixed particle position, as was shown in section 4. The latter is equivalent to gyro-averaging at fixed position of the guiding centre, $\boldsymbol{X} = \boldsymbol{x} - \boldsymbol{\rho}$, with the finite Larmor radius effects being neglected, e.g. $\langle \Phi(\boldsymbol{x}, t) \rangle_\alpha^{\boldsymbol{X}} = \langle \Phi(\boldsymbol{X} + \boldsymbol{\rho}, t) \rangle_\alpha^{\boldsymbol{X}} = \langle \Phi(\boldsymbol{X}, t) + (\boldsymbol{\rho} \cdot \boldsymbol{\nabla}) \Phi \rangle_\alpha^{\boldsymbol{X}} \approx \Phi(\boldsymbol{X}, t) \approx \Phi(\boldsymbol{x}, t)$ or $\langle \Phi(\boldsymbol{x}, t) \rangle_\alpha^{\boldsymbol{x}} = \Phi(\boldsymbol{x}, t)$. The fields, being functions of $\boldsymbol{x}$ and t, commute with the gyro-averaging operator at fixed $\boldsymbol{x}$. However, since the fields are not expanded in δ_* and $|\boldsymbol{\nabla}| \sim 1/L$ along and across the field lines when deriving the drift kinetic equation, certain effects associated with the rapid spatial variation are ordered out in the drift kinetic approach. Since the fields are not allowed to vary across the Larmor radius

length scales, we have to ensure that δ_* is an order smaller than Δ, i.e. the drift kinetic theory implicitly imposes limits on the poloidal component of the magnetic field: B_ϑ remains finite but is required to be smaller compared to B_0 for finite tokamak aspect ratio. While $B_\vartheta/B_0 \ll 1$ is typically a good approximation to describe a realistic D-shaped conventional tokamak geometry, it often becomes invalid for spherical tokamak equilibria. Indeed, the NTM is typically associated with the $q = (2-3)$ flux surfaces, and hence $B_\vartheta/B_0 \ll 1$ provides an ε limit, making the drift kinetic theory questionable for $\varepsilon > (0.4 - 0.5)$ and thus in certain cases not applicable for spherical tokamaks. To fully capture the $w \sim \rho$ (or $B_\vartheta \sim B_0$)

effects, the theory needs to be extended to gyrokinetics which we will address in future work.

6. Plasma response

6.1. DK-NTM formulation

To simplify the analysis below, we work in the island rest frame, which eliminates the time variation from the drift kinetic equation. Splitting the particle distribution function into the equilibrium Maxwell–Boltzmann piece and the perturbed piece, $g = \mathcal{O}(\Delta f_0)$, as discussed in [19], we obtain

$$
\begin{aligned}
&\frac{I}{qR^2}\left\{\frac{u}{B_0}\left[1 - I\frac{\partial}{\partial\psi}\Big|_{\vartheta,\varphi}\left(\frac{u}{\omega_c}\right) + \frac{\mu_0}{B_0^2}p'_{\text{eqm}}\frac{Iu}{\omega_c}\right] + \frac{I}{B_0^2}\frac{\partial\Phi}{\partial\psi}\Big|_{\vartheta,\xi} + \frac{s^2}{2\omega_c}\frac{\mu_0 j_\parallel}{B_0^2}\right\}\frac{\partial g}{\partial\vartheta}\Big|_{p_\varphi,\xi,\mu,V} \\
&+ \left\{\frac{u}{B_0}\left[(\boldsymbol{B}_1\cdot\boldsymbol{\nabla}p_\varphi) - \frac{I^2}{qR^2}\frac{u}{\omega_c}\left(I' + \frac{\mu_0}{B_0^2}p'_{\text{eqm}}I\right)\frac{\partial}{\partial\vartheta}\Big|_{\psi,\varphi}\left(\frac{u}{\omega_c}\right)\right] - \frac{I^2}{qR^2 B_0^2}\frac{\partial\Phi}{\partial\vartheta}\Big|_{p_\varphi,\xi} \right. \\
&\left. \quad + \frac{\partial\Phi}{\partial\xi}\Big|_{\psi,\vartheta} - \frac{s^2}{2\omega_c}\frac{\mu_0 j_\parallel}{B_0^2}\frac{I^2}{qR^2}\frac{\partial}{\partial\vartheta}\Big|_{\psi,\varphi}\left(\frac{u}{\omega_c}\right)\right\}\frac{\partial g}{\partial p_\varphi}\Big|_{\vartheta,\xi,\mu,V} \\
&+ \left\{\frac{u}{B_0}\left[\frac{I}{qR^2}q'_s\left(p_\varphi + \frac{Iu}{\omega_c}\right) + B_0^2\frac{\partial}{\partial\psi}\Big|_{\vartheta,\varphi}\left(\frac{u}{\omega_c}\right) + \vartheta'B_\vartheta^2\frac{\partial}{\partial\vartheta}\Big|_{\psi,\varphi}\left(\frac{u}{\omega_c}\right) - \mu_0 p'_{\text{eqm}}\frac{u}{\omega_c}\right] - \frac{\partial\Phi}{\partial\psi}\Big|_{\vartheta,\xi}\right\}\frac{\partial g}{\partial\xi}\Big|_{p_\varphi,\vartheta,\mu,V} \\
&+ \mu\frac{I}{qR^2}\left\{\frac{u}{B_0}\frac{\partial}{\partial\vartheta}\Big|_{\psi,\xi}\left(\frac{u}{\omega_c}\frac{\mu_0 j_\parallel}{B_0}\right) + \frac{s^2}{\omega_c}\frac{\mu_0}{B_0^2}p'_{\text{eqm}}\frac{I}{B_0^2}\frac{\partial B_0}{\partial\vartheta}\Big|_{\psi,\varphi}\right\}\frac{\partial g}{\partial\mu}\Big|_{\boldsymbol{x},V} \\
&- \frac{eZ}{m}\frac{u}{B_0}\frac{I}{qR^2}\frac{\partial\Phi}{\partial\vartheta}\Big|_{p_\varphi,\xi}\frac{\partial g}{\partial V\partial V}\Big|_{\boldsymbol{x},\mu} = Cg + \mathcal{O}\left(\Delta^3\frac{V_t}{R}f_0\right)
\end{aligned}
\tag{22}
$$

for the equation to be solved for g[8]. Here p_{eqm} is the equilibrium plasma pressure. In the absence of perturbations, we assume the plasma is in MHD equilibrium, i.e. $\boldsymbol{j}_0 \times \boldsymbol{B}_0 = \boldsymbol{\nabla}p_{\text{eqm}}$ and hence

$$
(\boldsymbol{b}_0\cdot\boldsymbol{\nabla})\boldsymbol{b}_0 - \boldsymbol{\nabla}\ln B_0 + (\boldsymbol{b}_0\cdot\boldsymbol{\nabla}\ln B_0)\boldsymbol{b}_0 = \frac{\mu_0}{B_0^2}\boldsymbol{\nabla}p_{\text{eqm}},
$$

where $\boldsymbol{j}_0$ is the equilibrium current density and $\boldsymbol{\nabla}p_{\text{eqm}} = p'_{\text{eqm}}\boldsymbol{\nabla}\psi$. Note, the perturbed magnetic field appears only in front of $\partial g/\partial p_\varphi$ since $|\boldsymbol{\nabla}_\perp| \sim 1/a$ when acting on equilibrium quantities and $|\boldsymbol{\nabla}_\perp| \sim 1/w$ when acting on perturbed quantities. Applying

$$
\begin{aligned}
\frac{\partial}{\partial V}\Big|_{\psi,\mu} &= \frac{\partial}{\partial V}\Big|_{p_\varphi,\mu} - \frac{IV}{u\omega_c}\frac{\partial}{\partial p_\varphi}\Big|_{V,\mu}, \\
\frac{\partial}{\partial\mu}\Big|_{\psi,V} &= \frac{\partial}{\partial\mu}\Big|_{p_\varphi,V} + \frac{IB_0}{u\omega_c}\frac{\partial}{\partial p_\varphi}\Big|_{\mu,V},
\end{aligned}
$$

---

[8] To obtain equation (22) it is convenient to rewrite the magnetic drift velocity in equation (15) as $\boldsymbol{V}_d = -\boldsymbol{u}\times\boldsymbol{\nabla}\left(\frac{u}{\omega_c}\right) + \frac{u^2}{\omega_c}\frac{\mu_0}{B}\boldsymbol{j}_\perp$.

we rewrite equation (22) in terms of $\{p_\varphi, \xi, \vartheta, \mu, V\}$:

$$
\begin{aligned}
&\frac{I}{qR^2}\left\{\frac{u}{B_0}\left[1 - I\frac{\partial}{\partial\psi}\Big|_{\vartheta,\varphi}\left(\frac{u}{\omega_c}\right) + \frac{\mu_0}{B_0^2}p'_{\text{eqm}}\frac{Iu}{\omega_c}\right] + \frac{I}{B_0^2}\frac{\partial\Phi}{\partial\psi}\Big|_{\vartheta,\xi} + \frac{s^2}{2\omega_c}\frac{\mu_0 j_\parallel}{B_0^2}\right\}\frac{\partial g}{\partial\vartheta}\Big|_{p_\varphi,\xi,\mu,V} \\
&\quad + \left\{\frac{u}{B_0}\left[(\boldsymbol{B}_1\cdot\boldsymbol{\nabla}p_\varphi) - \frac{I^2}{qR^2}\frac{u}{\omega_c}\left(I' + \frac{\mu_0}{B_0^2}p'_{\text{eqm}}I\right)\frac{\partial}{\partial\vartheta}\Big|_{\psi,\varphi}\left(\frac{u}{\omega_c}\right)\right] + \frac{\partial\Phi}{\partial\xi}\Big|_{\psi,\vartheta} \\
&\quad\quad + \frac{I^2}{qR^2B_0}\frac{s^2}{2\omega_c}\left[\frac{u}{\omega_c}\frac{\partial}{\partial\vartheta}\Big|_{\psi,\varphi}\left(\frac{\mu_0 j_\parallel}{B_0}\right) + \frac{s^2}{u}\frac{I}{\omega_c}\frac{\mu_0}{B_0^2}p'_{\text{eqm}}\frac{\partial B_0}{B_0\partial\vartheta}\Big|_{\psi,\varphi}\right]\right\}\frac{\partial g}{\partial p_\varphi}\Big|_{\vartheta,\xi,\mu,V} \\
&\quad + \left\{\frac{u}{B_0}\left[\frac{I}{qR^2}q'_s\left(p_\varphi + \frac{Iu}{\omega_c}\right) + B_0^2\frac{\partial}{\partial\psi}\Big|_{\vartheta,\varphi}\left(\frac{u}{\omega_c}\right) + \vartheta'B_\vartheta^2\frac{\partial}{\partial\vartheta}\Big|_{\psi,\varphi}\left(\frac{u}{\omega_c}\right) - \mu_0 p'_{\text{eqm}}\frac{u}{\omega_c}\right] - \frac{\partial\Phi}{\partial\psi}\Big|_{\vartheta,\xi}\right\}\frac{\partial g}{\partial\xi}\Big|_{p_\varphi,\vartheta,\mu,V} \\
&\quad + \mu\frac{I}{qR^2}\left\{\frac{u}{B_0}\frac{\partial}{\partial\vartheta}\Big|_{\psi,\xi}\left(\frac{u}{\omega_c}\frac{\mu_0 j_\parallel}{B_0}\right) + \frac{s^2}{\omega_c}\frac{\mu_0}{B_0^2}p'_{eqm}\frac{I}{B_0^2}\frac{\partial B_0}{\partial\vartheta}\Big|_{\psi,\varphi}\right\}\frac{\partial g}{\partial\mu}\Big|_{p_\varphi,\vartheta,\xi,V} \\
&\quad - \frac{eZ}{m}\frac{u}{B_0}\frac{I}{qR^2}\frac{\partial\Phi}{\partial\vartheta}\Big|_{p_\varphi,\xi}\frac{\partial g}{V\partial V}\Big|_{p_\varphi,\vartheta,\xi,\mu} = Cg + \mathcal{O}\left(\Delta^3\frac{V_t}{R}f_0\right).
\end{aligned}
$$

(23)

Switching to $\{p_\varphi, \xi, \vartheta, \lambda, V\}$, where λ is the pitch angle defined as $\lambda = 2\mu/V^2$ with

$$
\begin{aligned}
\frac{\partial}{\partial V}\Big|_\mu &= \frac{\partial}{\partial V}\Big|_\lambda - \frac{2\lambda}{V}\frac{\partial}{\partial\lambda}\Big|_V, \\
\frac{\partial}{\partial\mu}\Big|_V &= \frac{2}{V^2}\frac{\partial}{\partial\lambda}\Big|_V,
\end{aligned}
$$

and dividing both sides of the equation by $Iu/\left(B_0 R^2\right)$, we obtain

$$
\frac{1}{q}\frac{\partial g_0}{\partial\vartheta}\Big|_{p_\varphi,\xi,\lambda,V} = 0 \tag{24}
$$

for the $\mathcal{O}\left(\Delta^1 f_0\right)$ equation, where we have introduced

$$
g = g_0 + g_1 + \mathcal{O}\left(\Delta^3 f_0\right). \tag{25}
$$

From equation (24) we learn that the leading order plasma response to the magnetic island, g_0, is independent of ϑ at fixed p_φ. The $\mathcal{O}\left(\Delta^2 f_0\right)$ equation reads

$$
\begin{aligned}
&\frac{1}{q}\frac{\partial g_1}{\partial\vartheta}\Big|_{p_\varphi,\xi,\lambda,V} + \left\{\frac{R^2}{I}(\boldsymbol{B}_1\cdot\boldsymbol{\nabla}p_\varphi) + \frac{B_0 R^2}{Iu}\frac{\partial\Phi}{\partial\xi}\Big|_{\psi,\vartheta} - \frac{I^2}{2q}\left(\frac{I'}{I} + \frac{\mu_0}{B_0^2}p'_{\text{eqm}}\frac{V^2}{u^2}\right)\frac{\partial}{\partial\vartheta}\Big|_{\psi,\varphi}\left(\frac{u}{\omega_c}\right)^2\right\}\frac{\partial g_0}{\partial p_\varphi}\Big|_{\vartheta,\xi,\lambda,V} \\
&\quad + \left\{\frac{q'_s}{q}\left(p_\varphi + \frac{Iu}{\omega_c}\right) + \frac{R^2 B_0^2}{I}\frac{\partial}{\partial\psi}\Big|_{\vartheta,\varphi}\left(\frac{u}{\omega_c}\right) + \vartheta'\frac{R^2 B_\vartheta^2}{I}\frac{\partial}{\partial\vartheta}\Big|_{\psi,\varphi}\left(\frac{u}{\omega_c}\right)\right. \\
&\quad\quad \left. - \frac{uR^2}{I\omega_c}\mu_0 p'_{\text{eqm}} - \frac{R^2 B_0}{Iu}\frac{\partial\Phi}{\partial\psi}\Big|_{\vartheta,\xi}\right\}\frac{\partial g_0}{\partial\xi}\Big|_{p_\varphi,\vartheta,\lambda,V} \\
&\quad + \frac{\lambda}{q}\left\{\frac{\partial}{\partial\vartheta}\Big|_{\psi,\xi}\left(\frac{u}{\omega_c}\frac{\mu_0 j_\parallel}{B_0}\right) + \frac{s^2}{u\omega_c}\frac{\mu_0}{B_0^2}p'_{\text{eqm}}\frac{I}{B_0}\frac{\partial B_0}{\partial\vartheta}\Big|_{\psi,\varphi}\right\}\frac{\partial g_0}{\partial\lambda}\Big|_{p_\varphi,\vartheta,\xi,V} \\
&\quad - \frac{eZ}{m}\frac{1}{q}\frac{\partial\Phi}{\partial\vartheta}\Big|_{p_\varphi,\xi}\frac{\partial g_0}{V\partial V}\Big|_{p_\varphi,\vartheta,\xi,\lambda} + 2\frac{eZ}{m}\frac{\lambda}{qV^2}\frac{\partial\Phi}{\partial\vartheta}\Big|_{p_\varphi,\xi}\frac{\partial g_0}{\partial\lambda}\Big|_{p_\varphi,\vartheta,\xi,V} = \frac{R^2 B_0}{Iu}Cg_0 + \mathcal{O}\left(\Delta^3 f_0\right).
\end{aligned}
$$

(26)

Note, we split the ordering in equations (24) and (26) since the analysis is based on the extended drift kinetic equation, equation (13), that incorporates both the $\mathcal{O}\left(\delta_*^0\frac{V_t}{L}f_0\right)$ and

$\mathcal{O}\left(\delta_*^1\frac{V_t}{L}f_0\right)$ corrections, which results from equation (A.6). Integrating equation (26) over ϑ at fixed p_φ eliminates the first term on the left hand side of equation (26) and provides an equation for g_0:

$$\left\{ \left\langle \frac{R^2}{I} \left(\boldsymbol{B}_1 \cdot \boldsymbol{\nabla} p_\varphi \right) \right\rangle_\vartheta^{p_\varphi} + \left\langle \frac{B_0 R^2}{Iu} \frac{\partial \Phi}{\partial \xi} \right|_{\psi,\vartheta} \right\rangle_\vartheta^{p_\varphi}$$

$$- \frac{I^2}{2q} \left\langle \frac{\mu_0}{B_0^2} p'_{\text{eqm}} \frac{V^2}{u^2} \frac{\partial}{\partial \vartheta} \right|_{\psi,\varphi} \left(\frac{u}{\omega_c} \right)^2 \right\rangle_\vartheta^{p_\varphi} \right\} \frac{\partial g_0}{\partial p_\varphi} \bigg|_{\vartheta,\xi,\lambda,V}$$

$$+ \left\{ \left\langle \frac{q'_s}{q} \left(p_\varphi + \frac{Iu}{\omega_c} \right) \right\rangle_\vartheta^{p_\varphi} + \left\langle \frac{R^2 B_0^2}{I} \frac{\partial}{\partial \psi} \right|_{\vartheta,\varphi} \left(\frac{u}{\omega_c} \right) \right\rangle_\vartheta^{p_\varphi} \right.$$

$$+ \left\langle \vartheta' \frac{R^2 B_\vartheta^2}{I} \frac{\partial}{\partial \vartheta} \right|_{\psi,\varphi} \left(\frac{u}{\omega_c} \right) \right\rangle_\vartheta^{p_\varphi}$$

$$\left. - \left\langle \frac{uR^2}{I\omega_c} \mu_0 p'_{\text{eqm}} \right\rangle_\vartheta^{p_\varphi} - \left\langle \frac{R^2 B_0}{Iu} \frac{\partial \Phi}{\partial \psi} \right|_{\vartheta,\xi} \right\rangle_\vartheta^{p_\varphi} \right\} \frac{\partial g_0}{\partial \xi} \bigg|_{p_\varphi,\vartheta,\lambda,V}$$

$$+ \frac{\lambda}{q} \left\langle \frac{s^2}{u\omega_c} \frac{\mu_0}{B_0^2} p'_{\text{eqm}} \frac{I}{B_0} \frac{\partial B_0}{\partial \vartheta} \right|_{\psi,\varphi} \right\rangle_\vartheta^{p_\varphi} \frac{\partial g_0}{\partial \lambda} \bigg|_{p_\varphi,\vartheta,\xi,V}$$

$$= \left\langle \frac{R^2 B_0}{Iu} C \right\rangle_\vartheta^{p_\varphi} g_0 + \mathcal{O}\left(\Delta^3 f_0 \right). \tag{27}$$

Equation (27) with equation (20) extends equation 14 of [19] to a finite beta case. The orbit-averaging operator at fixed p_φ, $\langle \ldots \rangle_\vartheta^{p_\varphi}$, is defined as in equation 16 of [19]:

$$\langle \ldots \rangle_\vartheta^{p_\varphi} = \begin{cases} \frac{1}{2\pi} \int_{-\pi}^{\pi} \ldots d\vartheta, & \lambda \leqslant \lambda_c \\ \frac{1}{4\pi} \sum_\sigma \sigma \int_{-\vartheta_b}^{\vartheta_b} \ldots d\vartheta, & \lambda > \lambda_c. \end{cases}$$

Here $\sigma \equiv u/|u| = \pm 1$, and λ_c is the trapped-passing boundary. The bounce points, $\vartheta = \vartheta_b$, are provided by the condition: $u(\vartheta_b) = 0$. Note, to switch from equations (26) to (27) we have used the result

$$\frac{\partial}{\partial \vartheta} \bigg|_{p_\varphi} = \frac{\partial}{\partial \vartheta} \bigg|_\psi + \frac{\partial}{\partial \vartheta} \bigg|_{p_\varphi} \left(\frac{Iu}{\omega_c} \right) \frac{\partial}{\partial \psi} \bigg|_\vartheta$$

$$= \frac{\partial}{\partial \vartheta} \bigg|_\psi + \frac{\partial}{\partial \vartheta} \bigg|_\psi \left(\frac{Iu}{\omega_c} \right) \frac{\partial}{\partial \psi} \bigg|_\vartheta + \mathcal{O}\left(\delta_*^2 \Theta^{-2} \right)$$

when acting on equilibrium quantities.

To analyse equation (27) further, we introduce the dimensionless system considered in equation 19 of [19]. Equation (27) then becomes

$$\left[\frac{\hat{w}}{\hat{L}_q} \hat{p}_\varphi \Theta \left(\lambda_c - \lambda \right) - \hat{\rho}_\vartheta \hat{\omega}_D - \frac{1}{2} \left\langle \frac{R^2 B_0^2}{I^2} \frac{\hat{\rho}_\vartheta}{\hat{u}} \frac{\partial \hat{\Phi}}{\partial \hat{\psi}} \right|_{\vartheta,\xi} \right\rangle_\vartheta^{p_\varphi} \right] \frac{\partial g_0}{\partial \xi} \bigg|_{p_\varphi,\vartheta,\lambda,V}$$

$$\left\{ \frac{1}{2} \left\langle \frac{R^2 B_0^2}{I^2} \frac{\hat{\rho}_\vartheta}{\hat{u}} \frac{\partial \hat{\Phi}}{\partial \xi} \right|_{\psi,\vartheta} \right\rangle_\vartheta^{p_\varphi} + \frac{1}{q} \left\langle \hat{\rho}_\vartheta^2 \left(\hat{\beta}' + 2\hat{\beta} \frac{\hat{w}}{\hat{L}_B} \right) \frac{\hat{V}^2}{\hat{u}} \left(\hat{u} + \frac{\lambda B_0}{2} \frac{\hat{V}^2}{\hat{u}} \right) \frac{\partial B_0}{B_0 \partial \vartheta} \right|_{\psi,\varphi} \right\rangle_\vartheta^{p_\varphi}$$

$$\left. - \frac{\hat{w}}{4\hat{L}_q} \left\langle \text{n} \frac{B_\vartheta^2}{B_\varphi B_0} \left(1 + \frac{q_s}{q} \frac{B_\varphi^2}{B_\vartheta^2} \right) \sin\left(\text{n}\xi\right) - \frac{1}{q} \frac{I}{R^2 B_0^2} \frac{\partial (RB_0)}{\partial \vartheta} \right|_{\psi,\varphi} \cos\left(\text{n}\xi\right) \right\rangle_\vartheta^{p_\varphi} \right\} \frac{\partial g_0}{\partial \hat{p}_\varphi} \bigg|_{\vartheta,\xi,\lambda,V}$$

$$+ \frac{\lambda}{q} \left\langle \hat{\rho}_\vartheta \frac{\hat{s}^2}{\hat{u}} \left(\hat{\beta}' + 2\hat{\beta} \frac{\hat{w}}{\hat{L}_B} \right) \frac{\partial B_0}{B_0 \partial \vartheta} \right|_{\psi,\varphi} \right\rangle_\vartheta^{p_\varphi} \frac{\partial g_0}{\partial \lambda} \bigg|_{p_\varphi,\vartheta,\xi,V} = \hat{C} g_0 + \mathcal{O}\left(\Delta^3 f_0 \right). \tag{28}$$

Here hats denote normalised quantities: $\hat{\psi} = \psi/w_\psi$, $\hat{p}_\varphi = p_\varphi/w_\psi$, $\hat{w} = w_\psi/\psi_s$, $\hat{V} = V/V_t$ and $\hat{u} = u/V_t$. $\hat{\rho}_\vartheta = IV_t/(\omega_c w_\psi)$ is the normalised particle poloidal Larmor radius. $\hat{\Phi} = e\Phi/T_e$ is the normalised perturbed electrostatic potential with e and T_e being the electron charge and equilibrium temperature, respectively. We have introduced $\hat{\beta}'$ and $\hat{\vartheta}'$ as $\hat{\beta} \equiv \mu_0 p_{\text{eqm}}/B_0^2$ and ϑ differentiated with respect to $\hat{\psi}$. $\hat{C}$ is the normalised right hand side collision operator of equation (27). The normalised drift frequency is defined as

$$\hat{\rho}_\vartheta \hat{\omega}_D = - \frac{\hat{w}}{\hat{L}_q} \langle \hat{\rho}_\vartheta \hat{u} \rangle_\vartheta^{p_\varphi} + \left\langle \frac{R^2 B_0^2}{I^2} \frac{\hat{\rho}_\vartheta \hat{w}}{\hat{L}_B} \left(\hat{u} + \frac{\lambda B_0}{2} \frac{\hat{V}^2}{\hat{u}} \right) \right\rangle_\vartheta^{p_\varphi}$$

$$+ \left\langle \hat{\vartheta}' \frac{R^2 B_\vartheta^2}{I^2} \hat{\rho}_\vartheta \left(\hat{u} + \frac{\lambda B_0}{2} \frac{\hat{V}^2}{\hat{u}} \right) \frac{\partial B_0}{B_0 \partial \vartheta} \right|_{\psi,\varphi} \right\rangle_\vartheta^{p_\varphi}$$

$$+ \left\langle \frac{R^2 B_0^2}{I^2} \hat{\rho}_\vartheta \hat{u} \left(\hat{\beta}' + 2\hat{\beta} \frac{\hat{w}}{\hat{L}_B} \right) \right\rangle_\vartheta^{p_\varphi}. \tag{29}$$

Θ denotes the Heaviside step function. $\hat{L}_q$ and $\hat{L}_B$ are the normalised safety factor and equilibrium magnetic field length scales, respectively: $\hat{L}_q^{-1} = (q'_s/q)\psi_s$ and $\hat{L}_B^{-1} = (\psi_s/B_0)\partial B_0/\partial \psi$.

6.2. Drift magnetic islands. RDK-NTM formulation

Equation (28) is equivalent to

$$\left[\frac{\hat{w}}{\hat{L}_q} \hat{p}_\varphi \Theta \left(\lambda_c - \lambda \right) - \hat{\rho}_\vartheta \hat{\omega}_D \right.$$

$$\left. - \frac{1}{2} \frac{\partial}{\partial \hat{p}_\varphi} \bigg|_{\vartheta,\xi} \left\langle \frac{R^2 B_0^2}{I^2} \frac{\hat{\rho}_\vartheta}{\hat{u}} \hat{\Phi} \right\rangle_\vartheta^{p_\varphi} \right] \frac{\partial g_0}{\partial \xi} \bigg|_{S,\vartheta,\lambda,V}$$

$$= \hat{C} g_0 - \frac{\lambda}{q} \left\langle \hat{\rho}_\vartheta \frac{\hat{s}^2}{\hat{u}} \left(\hat{\beta}' + 2\hat{\beta} \frac{\hat{w}}{\hat{L}_B} \right) \frac{\partial B_0}{B_0 \partial \vartheta} \right|_{\psi,\varphi} \right\rangle_\vartheta^{p_\varphi} \frac{\partial g_0}{\partial \lambda} \bigg|_{p_\varphi,\vartheta,\xi,V}$$

$$+ \mathcal{O}\left(\Delta^3 f_0 \right), \tag{30}$$

where

$$S = \frac{\hat{w}}{4\hat{L}_q} \left[2\left(\hat{p}_\varphi - \frac{\hat{\rho}_\vartheta \hat{\omega}_D \hat{L}_q}{\hat{w}}\right)^2 - \left\langle \frac{B_\vartheta^2}{B_\varphi B_0}\left(1 + \frac{B_\varphi^2}{B_\vartheta^2}\right) \right. \right.$$

$$\left. \cos(\mathrm{n}\xi) + \frac{1}{\mathrm{m}} \frac{I}{R^2 B_0^2} \left. \frac{\partial(R B_0)}{\partial \vartheta}\right|_{\psi,\varphi} \sin(\mathrm{n}\xi) \Big\rangle_\vartheta^{p_\varphi} \right] \Theta(\lambda_c - \lambda)$$

$$- \hat{\rho}_\vartheta \hat{\omega}_D \hat{p}_\varphi \Theta(\lambda - \lambda_c) - \frac{1}{2}\left\langle \frac{R^2 B_0^2}{I^2} \frac{\hat{\rho}_\vartheta}{\hat{u}} \hat{\Phi} \right\rangle_\vartheta^{p_\varphi}$$

$$- \frac{\mathrm{n}}{\mathrm{m}} \left\langle \hat{\rho}_\vartheta^2 \left(\hat{\beta}' + 2\hat{\beta}\frac{\hat{w}}{\hat{L}_B}\right) \frac{\hat{V}^2}{\hat{u}} \left(\hat{u} + \frac{\lambda B_0}{2}\frac{\hat{V}^2}{\hat{u}}\right) \left.\frac{\partial B_0}{B_0 \partial \vartheta}\right|_{\psi,\varphi} \right\rangle_\vartheta^{p_\varphi} \xi,$$

$$\tag{31}$$

provided all equilibrium quantities are slowly varying functions of ψ that can be evaluated at ψ_s and

$$\left\langle \frac{R^2 B_0^2}{I^2} \frac{\hat{\rho}_\vartheta}{\hat{u}} \left.\frac{\partial \hat{\Phi}}{\partial \hat{\psi}}\right|_{\vartheta,\xi} \right\rangle_\vartheta^{p_\varphi} = \left.\frac{\partial}{\partial \hat{p}_\varphi}\right|_{\vartheta,\xi} \left\langle \frac{R^2 B_0^2}{I^2} \frac{\hat{\rho}_\vartheta}{\hat{u}} \hat{\Phi} \right\rangle_\vartheta^{p_\varphi},$$

$$\left\langle \frac{R^2 B_0^2}{I^2} \frac{\hat{\rho}_\vartheta}{\hat{u}} \left.\frac{\partial \hat{\Phi}}{\partial \xi}\right|_{\psi,\vartheta} \right\rangle_\vartheta^{p_\varphi} = \left.\frac{\partial}{\partial \xi}\right|_{\hat{p}_\varphi,\vartheta} \left\langle \frac{R^2 B_0^2}{I^2} \frac{\hat{\rho}_\vartheta}{\hat{u}} \hat{\Phi} \right\rangle_\vartheta^{p_\varphi}.$$

The normalised electrostatic potential, $\hat{\Phi}$, in equations (28) and (30) is to be determined iteratively by balancing the ion and electron densities to ensure plasma quasi-neutrality [19].[9] As was demonstrated in [19], this allows one to retain both the ion and electron effects on the pressure gradient physics across the magnetic island. Following [9, 16–19], we close the system with a collision operator that conserves particles and momentum, making equations (30)/(28) an integro-differential system rather than simply a differential equation. The solution technique reproduces the one discussed in [16–18] for the 4D $(p_\varphi, \xi, \lambda, V)$ DK-NTM and in [19] for the low collisional 3D (S, λ, V) RDK-NTM approach. To solve for the distribution function as a function of S, in [19] we employ weak collisional dissipation in λ space, excluding a thin boundary layer that surrounds the trapped-passing boundary. In the trapped-passing boundary layer, the perturbative treatment of collisions becomes invalid since collisional dissipation proportional to steep gradients in pitch angle becomes comparable to parallel streaming. Therefore, there we solve the 4D DK-NTM equation, equation (28), exploiting the layer thinness. This then resolves the discontinuity in the distribution function and its derivatives across the trapped-passing boundary that originates from different orbit averaging procedures for passing and trapped particles in the left hand side of equation (28).

We note that in contrast to equations 14 and 20 of [19] and equation 32 of [18], equations (28) and (30) contain some additional anisotropy associated with the magnetic moment variation of the Vlasov operator in equation (7). The corresponding term in the drift kinetic equation is proportional to β and

[9] Note, the perturbed potential associated with the magnetic island is $\Phi_1 \sim \Delta\Phi_0$. Here Φ_0 is the equilibrium potential and is assumed to be a function of ψ only.

thus is typically ordered out for most applications. However, to allow an extension to a high beta plasma we must allow finite β values. While the DK-NTM approach based on equation (28) retains collisions at the $\mathcal{O}(\Delta^2 f_0)$ order for a full range of λ variation and hence does not require any additional limits on β and $\hat{\beta}'$, the RDK-NTM approach operates in S space and treats collisions perturbatively. To allow the leading order distribution function, g_0, to be constant on the contours of fixed S, similar to [19], we must require

$$\nu^* \sim \frac{1}{\varepsilon}\left(\hat{\beta}' + 2\hat{\beta}\frac{\hat{w}}{\hat{L}_B}\right), \tag{32}$$

together with $\nu/\varepsilon k_\parallel V_t \ll 1$, where ν^* is the plasma collisionality, ν is the particle collision frequency and $k_\parallel$ is the parallel wave number, for the perturbative treatment of collisions to be valid. Typical values of ν^* in the RDK-NTM model are $(10^{-4} - 10^{-2})$, therefore β is allowed to vary between $(10^{-2} - 1)$, provided $w \sim \rho_{bi} \sim$ cm and $a \sim$ m (metres) with $\Delta \sim 10^{-2}$. At the same time, no sharp spatial variations are allowed in $\hat{\beta}'$ in the RDK-NTM model.

In the limit of equations (21) and (32), the contours of constant S in accordance with equation (31) reproduce the shape of magnetic islands for passing particles, similar to the small inverse aspect ratio, circular cross section limit considered in [19]. The non-zero values of β and $\hat{\beta}'$ increase the magnitude of the radial shift of the constant S island compared to the magnetic island in equation (29). The effect associated with the finite β on this radial shift is weaker as β also appears implicitly in equation (29) via $\hat{L}_B^{-1}$. As can be seen from equation (31), the drift island separatrix position also depends on B_ϑ, which makes drift islands wider for stronger B_ϑ, e.g. see figure 1. This then increases the flattening region of the particle distribution function at $\sigma = \pm 1$, which together with the larger radial shift in S for finite β and $\hat{\beta}'$ will further enhance the stabilising threshold mechanism provided by passing particles.

6.3. Curvature effects

To describe non-circular shifted finite aspect ratio plasma equilibria (e.g. see Figure 2 (*a*)), we employ the 'Miller' formalism [25]. It provides a local tokamak equilibrium model in terms of nine parameters, including inverse aspect ratio, elongation κ, triangularity δ, safety factor and magnetic shear. To specify the shape of the plasma boundary, we use the conventional parametrisation for the D-shaped plasmas [25, 26]:

$$R = R_0(r) + r\cos(\vartheta + x\sin\vartheta),$$
$$Z = \kappa r \sin\vartheta, \tag{33}$$

where $x = \arcsin\delta$, and $R_0(r)$ includes the Shafranov shift. The poloidal magnetic field component is parametrised based on the assumption that the nearby inner closed flux surfaces are described by equation (33) but with modified values of R_0, κ and δ. It is given by equation 37 of [25]. This makes B_ϑ dependent on κ, δ, s_κ (elongation shear), s_δ (triangularity shear), ε as well as β_ϑ (ratio of plasma pressure to poloidal
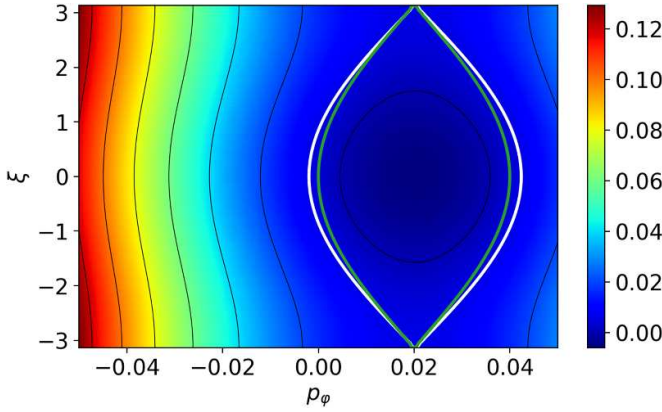
Figure 1. Contours of constant S in the (p_φ, ξ) plane in the absence of the electrostatic potential and the parallel drift effects for deeply passing particles. The plasma parameters are $w = \rho_{\vartheta i} = 0.02\, r_s$, $V = V_t$, $\hat{L}_q = 1$, $\sigma = -1$ with the normalised equilibrium density and temperature gradient length scales respectively $L_n/\psi_s = 1$, $L_T/\psi_s = 1$ [19] for the m = 2, n = 1 mode. The white curve indicates the position of the drift island separatrix at $S = \frac{\hat{w}}{4\hat{L}_q} \left\langle \frac{B_\vartheta^2}{B_\varphi B_0} \left(1 + \frac{B_\varphi^2}{B_\vartheta^2}\right) \right\rangle_\vartheta^{p_\varphi}$. B_ϑ is reconstructed from the Miller equilibrium model with $\varepsilon = 0.1$, $\delta = -0.3$ (triangularity) and $\kappa = 1.0$ (elongation) [25]. The green curve represents the drift island separatrix in the small inverse aspect ratio tokamak approximation at $S = \hat{w}/4\,\hat{L}_q$ in the absence of B_ϑ.

magnetic field pressure) and the internal inductance l_i via $\partial_r R_0$ [25].[10]

We note that while the Miller equilibrium provides a convenient analytic model to describe the D-shaped plasma, the tokamak equilibrium configuration employed to provide the coefficients in equations (28) and (30) can be generalised (provided $B_\vartheta/B_0 \ll 1$) and can be replaced with one reconstructed using existing equilibrium solvers (e.g. [28, 29] etc). For most of the cases considered below, we employ a theoretical Miller geometry to explore, in a qualitative way, the impact of plasma shaping on the threshold. To provide experimental evidence for our theory, we also study EAST discharge (number 91972) with the 2/1 NTM excited by resonant magnetic perturbations, using a real experimental equilibrium with plasma parameters consistent with the location of the mode.

6.3.1. Triangularity effects. In this subsection we investigate the effects of triangularity, including negative triangularity equilibria, on the NTM behaviour. The triangularity enters the equilibrium magnetic field via equation (33) and therefore influences the trapped particle physics via bounce points, e.g. see figure 2(c). δ also enters equation (29) which, in turn, influences the radial shift of drift islands for passing particles in equation (31). As can be seen from Figure 2(b), $\hat{\omega}_D$ increases

---

[10] The parameter $\partial_r R_0$ written in terms of β_ϑ and l_i is derived in [27] for large aspect ratios. A comparison with numerical equilibria demonstrates that the result of [27] remains relatively accurate at finite aspect ratio [25].

at decreasing δ and hence the negative triangularity effect enhances the shift of the drift islands relative to the magnetic island. This is then expected to increase the stabilising effect for small islands of widths comparable to the poloidal Larmor radius [19]. Therefore, one would expect to see an increase in the NTM threshold island width for lower δ and even perhaps expect the discharges to be free of NTMs at sufficiently negative values of δ.
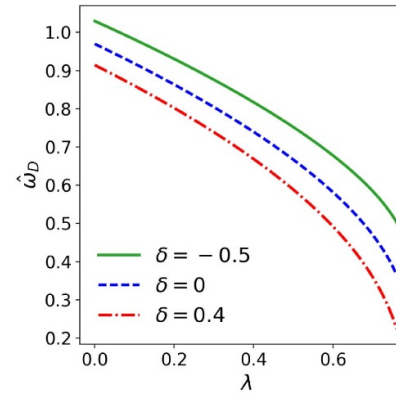
In [19, 30] we consider how the parallel flows that contribute to Ampère's law parallel to the field lines and thus to the NTM dispersion relation, vary with $\rho_{\vartheta i}/w$. For small $\rho_{\vartheta i}/w$, the result is consistent with the conventional theory of NTMs, i.e. the parallel current is zero inside the magnetic island of width $w \gg \rho_{\vartheta i}$ which provides a strong NTM drive. In contrast, as the island width decreases towards values comparable to the ion poloidal Larmor radius, $w \gtrsim \rho_{\vartheta i}$, we find that there is some negative (stabilising) flow that penetrates into the island near the X-points (e.g. see figures 3(b) and 4(b)). It spreads further into the island region with increasing $\rho_{\vartheta i}/w$ and competes with growing positive (destabilising) flows outside the magnetic island separatrix. In figures 3 and 4 we investigate this effect further at different triangularities. Positive triangularity enhances the destabilising flows outside the separatrix (see figures 3(c) and 4(c)), while negative triangularity enhances stabilising flows inside the island (see figures 3(a) and 4(a)) as one would expect from figure 2(b) and equation (29).

To calculate the threshold island width, we employ the standard NTM dispersion relation (see equations 32–34 of [19]), based on Ampère's law and the magnetic field perturbation in equations (18) and (19). For a single isolated stationary magnetic island chain, the classical tearing mode stability parameter, Δ', is balanced against the contribution associated with the resistive layer currents calculated here (i.e. bootstrap, curvature and polarisation effects) to provide the threshold. As we assume no equilibrium electric field, Δ_{pol} only enters via the perturbed electrostatic potential required to maintain quasi-neutrality. Calculation of Δ', which depends on the global equilibrium properties and can generally be treated as an input in our model, is beyond the scope of this work. Hence, rather than evaluating the experimental threshold island width, we define the threshold as a critical island half-width, w_c, above which the localised NTM drives are destabilising. For $w < w_c$, the island can only be driven by a classical drive, $\Delta' > 0$, which then might be interpreted as a 'classical' tearing mode. However, we find that the neoclassical contributions are typically much larger than Δ' (which is characterised by $-2m/r_s$ for widths only slightly different from $2\,w_c$ – in that case the distinction between the experimental threshold and w_c is negligible. Figure 5 shows how different values of plasma triangularity influence the NTM threshold island half-width, w_c, for a model theoretical Miller geometry in figures 5 (a) and (b), and for the experimental equilibrium reconstruction in figure 5(c). The threshold island width, $2w_c$, is found to increase with decreasing plasma triangularity, e.g. from $1.82\rho_{bi}$ at $\delta = 0.42$ to $2.90\rho_{bi}$ at $\delta = -0.5$ in figure 5(b).
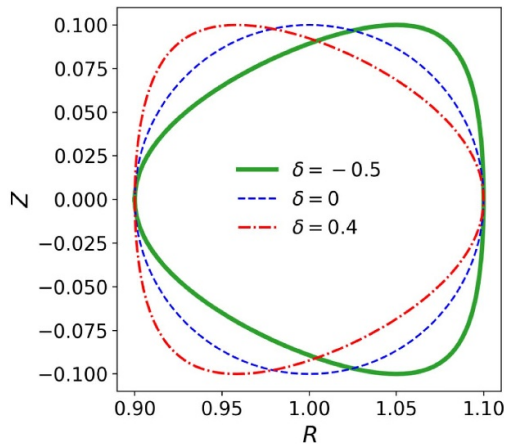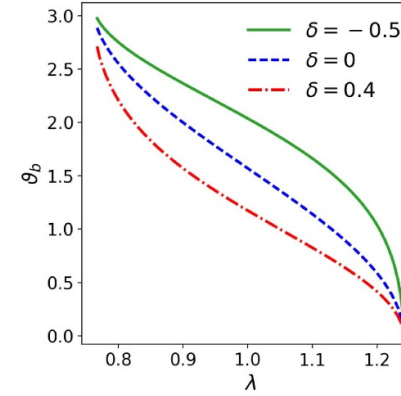
(a) The Miller equilibrium (R, Z) poloidal cross section at $\kappa = 1$ and different δ. R and Z are normalised to R_0.

(b) The normalised drift frequency, $\hat{\omega}_D$, plotted as a function of pitch angle, λ, at different δ; $\kappa = 1$. The $\delta = 0$ curve corresponds to the circular poloidal cross section employed in [18, 19].

(c) The trapped particle bounce point, ϑ_b, plotted as a function of pitch angle, λ, at different δ; $\kappa = 1$. The $\delta = 0$ curve corresponds to the circular poloidal cross section employed in [18, 19].

Figure 2. The triangularity effects on the passing (via $\hat{\omega}_D$) and trapped (via ϑ_b) particles.
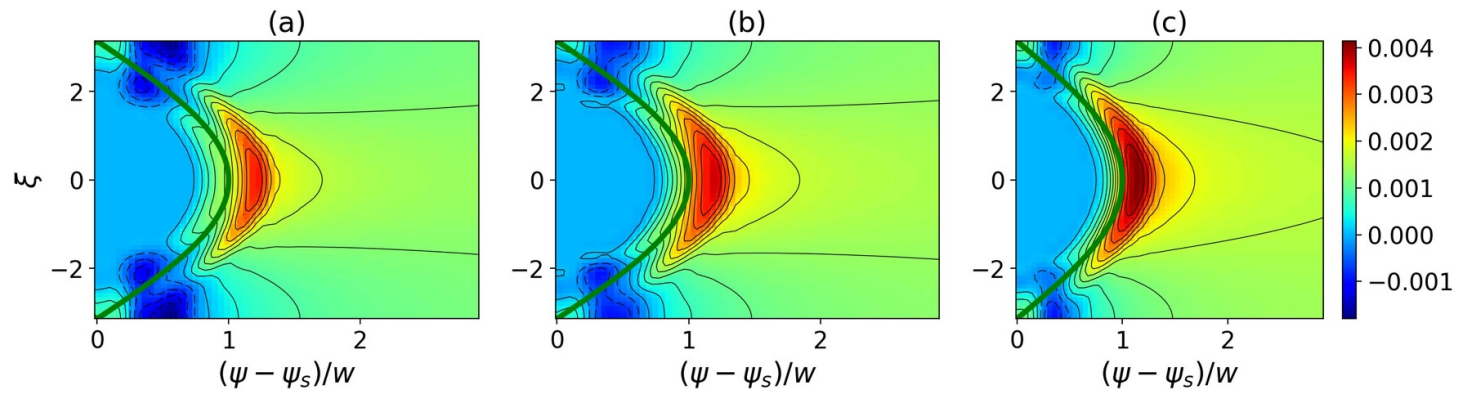
Figure 3. Colour contours showing the ion parallel flow, $u_{\parallel i}$, in the (ψ, ξ) plane at $\rho_{\vartheta i}/w = 0.35$ at $\delta = -0.5$ (*a*), $\delta = 0$ (*b*) and $\delta = 0.42$ (*c*) in the absence of the parallel drift effects. $u_{\parallel i}$ is normalised to the ion thermal velocity. The parameters are $V = V_t$, $\varepsilon = 0.1$, $\kappa = 1.7$, $\hat{L}_q = 1$ with the normalised equilibrium density and temperature gradient length scales $L_n/\psi_s = 1$, $L_T/\psi_s = 1$ for the m $= 2$, n $= 1$ mode. The green curve indicates the position of the magnetic island separatrix. (*b*) is equivalent to a zero triangularity plasma considered in [19].
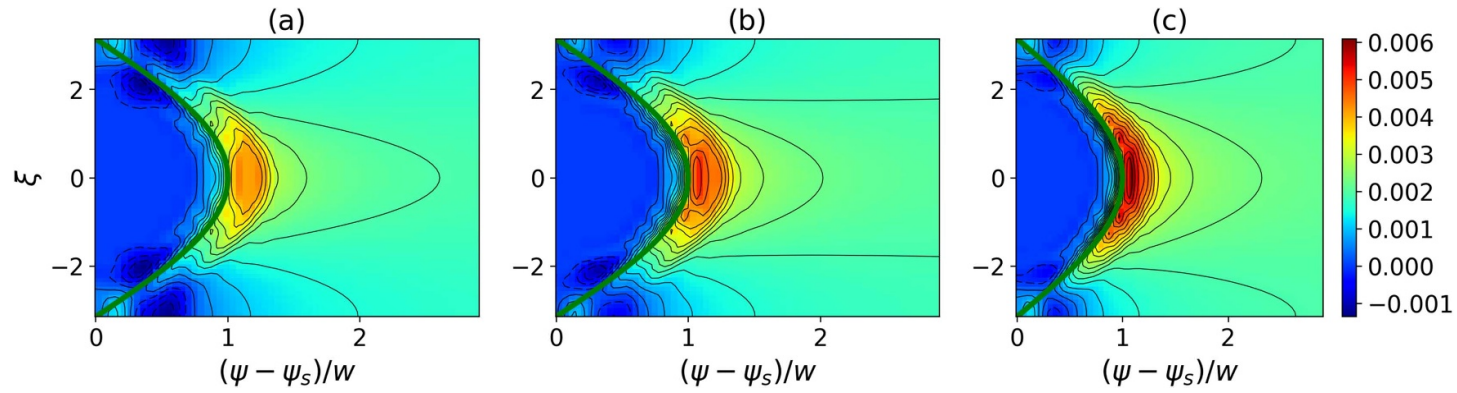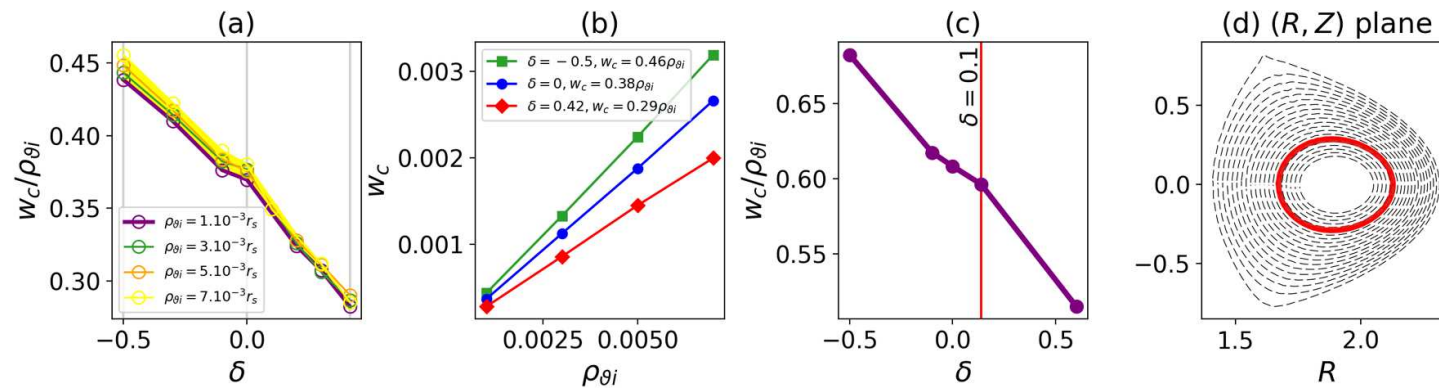
Figure 4. Colour contours showing the parallel current, $j_\parallel$, in the (ψ, ξ) plane at $\rho_{\vartheta i}/w = 0.35$ at $\delta = -0.5$ (*a*), $\delta = 0$ (*b*) and $\delta = 0.42$ (*c*) in the absence of the parallel drift effects. $j_\parallel$ is normalised to $e n_0 V_{ti}$, where n_0 is the equilibrium density and V_{ti} is the ion thermal velocity. The parameters are $V = V_t$, $\varepsilon = 0.1$, $\kappa = 1.7$, $\hat{L}_q = 1$ with the normalised equilibrium density and temperature gradient length scales $L_n/\psi_s = 1$, $L_T/\psi_s = 1$ for the m = 2, n = 1 mode. The green curve indicates the position of the magnetic island separatrix. (*b*) is equivalent to a zero triangularity plasma considered in [19].

Figure 5. The triangularity effects on the NTM threshold for the m = 2, n = 1 mode: (*a*) and (*b*) for a model theoretical Miller geometry and in the absence of the parallel drift effects, corresponding to figures 3 and 4; (*c*) for an example equilibrium reconstruction plotted in (*d*) and in the presence of the parallel drift effects. (*a*) $w_c/\rho_{\vartheta i}$ plotted as a function of δ at different $\rho_{\vartheta i}$, (*b*) w_c plotted as a function of $\rho_{\vartheta i}$ at different δ at $V = V_t$, $\nu^* = 10^{-4}$, $\beta_{\vartheta} = 0.5$ with the plasma shape characterised by $\varepsilon = 0.1$, $\kappa = 1.7$. (*c*) $w_c/\rho_{\vartheta i}$ plotted as a function of δ at $V = V_t$, $\nu^* = 10^{-3}$, $\beta_{\vartheta} = 0.7$ with $\varepsilon = 0.13$, $\kappa = 1.25$, $s_{\kappa} = 0.07$ and $\hat{L}_q = 0.29$ at the 2/1 rational surface. In (*c*) $\delta = 0.1$ corresponds to the experimental value at the 2/1 rational surface shown as a red curve in (*d*) (EAST, discharge number 91972). The experimental equilibrium is fitted to the Miller parametrisation, and then δ is varied in that fit to provide the scan shown in (*c*). Note, w_c and $\rho_{\vartheta i}$ are in r_s units.

6.3.2. Triangularity dependence of the 2/1 NTM onset relative frequency in DIII-D plasmas.

In order to explore the parameter dependence of triggering mechanisms and drivers of the robustly growing regime, we calculated the 2/1 onset relative frequency with respect to a group of plasma parameters (X^i) and shape parameters, including elongation (κ) and triangularity (δ).

We assume that every $\Delta\tau \approx 100$ ms window of plasma can be considered as an independent measurement point. Every stable plasma is then subdivided into $\Delta\tau$ windows in the current flattop, and time averages of X^i within each window are collected into the database. This is then repeated for the stable part of the unstable discharges, defined as $t < t_{\rm onset} - \Delta\tau$, and compiled into the same stable database. Next, the unstable database of X^i is assembled from a single $\Delta\tau$ window preceding $t_{\rm onset}$ in each unstable discharge. This method yields an unstable database of 2645 points and a stable database of 509 535 points for each X^i. This method produces a large database for each X^i. However, it does not guarantee that the parameters vary independently. The latter can be tested by the pair-correlation coefficient of the X^i and X^j variables in the stable database $(C^s_{X^i,X^j})$. Such correlations can exist either due to physical relationships between the variables or due to preferred operational choices in the analysed DIII-D campaigns (the parameter space is not scanned uniformly, but the experiments are driven by physics goals). We consider therefore the possibility that the sample sets of the X^i parameters are not all and not fully independent from each other. We find a relatively weak correlation though between δ, κ and β_ϑ: $C^s_{\delta,\beta_\theta} = 0.28$, $C^s_{\delta,\kappa} = 0.29$.

We define the 2/1 onset relative frequency $(\Omega(X^i))$ as:

$$\Omega(X^i) = \frac{H_\alpha(X^i)}{H_\gamma(X^i)}, \tag{34}$$

where $H_\alpha(X^i)$ and $H_\beta(X^i)$ are the histograms of X_i calculated from the unstable and stable database, respectively, and $H_\gamma(X^i) = H_\alpha(X^i) + H_\beta(X^i)$ is the histogram of the union of the stable and unstable databases. All histograms are calculated in 75 points with respect to X^i and the ranges of the X^i are chosen to cover most of the DIII-D operational space.

Figure 6(*a*) shows $\bar{H}_\alpha(X^i)$ and $\bar{H}_\beta(X^i)$ for $X^i = \delta$, the normalized histograms of the unstable and stable datasets of δ, respectively:

$$\bar{H}_\alpha(X^i_k) = \frac{H_\alpha(X^i_k)}{\sum_k H_\beta(X^i_k)} \tag{35}$$

$$\bar{H}_\beta(X^i_k) = \frac{H_\beta(X^i_k)}{\sum_k H_\beta(X^i_k)} \tag{36}$$

here k indexes the value of the X^i variable . The line graph in figure 6(*b*) shows $\Omega(\delta)$, and $H_\gamma(\delta)$ is shown as a shaded area in addition. The mode onset is sensitive to the parameter X_i where $|\partial_{X_i}\Omega| > 0$. Given the bin size, the sensitivity carries impact at the X^i_k value if $H_\gamma(X^k_i) \gtrsim 1\%$, which covers over 90% of the plasmas.
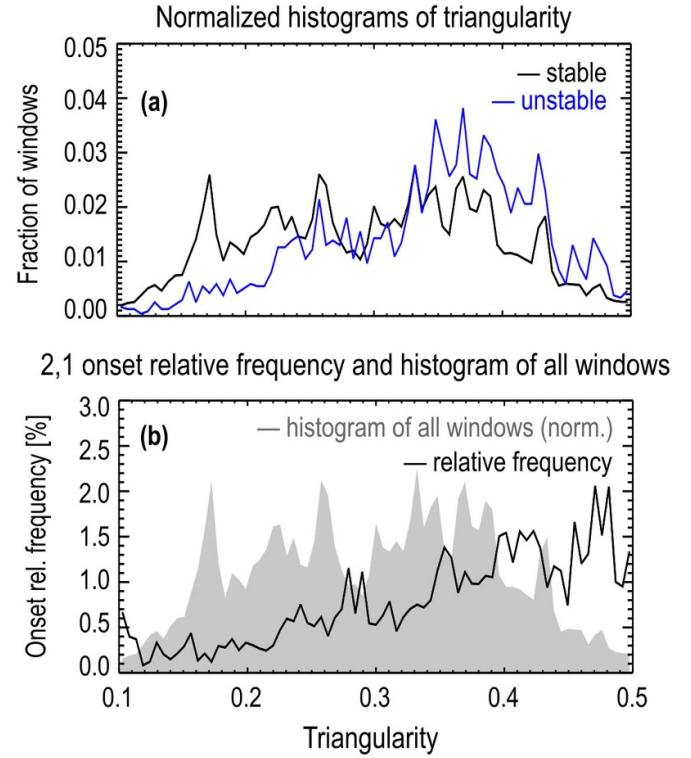

Figure 6. (*a*) Histograms of stable and unstable plasmas, (*b*) 2/1 NTM onset relative frequency vs. δ.

As can be seen from figure 6(*b*), the 2/1 island onset relative frequency increases with plasma triangularity, i.e. $\partial_\delta\Omega(\delta) > 0$, which indicates that the higher triangularity plasma is more prone to the 2/1 islands in DIII-D. The latter is in agreement with the RDK-NTM prediction discussed in section 6.3.1, i.e. positive triangularity enhances destabilising flows, increasing the NTM drive.

6.3.3. Finite aspect ratio effects.

In this subsection we investigate the aspect ratio effects on the NTM threshold physics, extending the results of [19] obtained in the small inverse aspect ratio tokamak approximation (see figure 9 of [19]). In figures 4(*b*) and 7 we show contours of the parallel current density at different ε. The larger inverse aspect ratio is found to further enhance the stabilising flows around the magnetic island separatrix in addition to the effects of negative triangularity discussed above. In figure 8 we plot $w_c/\rho_{\vartheta i}$ as a function of ε. As can be seen from figure 8, w_c is proportional to $\varepsilon^{1/2}\rho_{\vartheta i} = \rho_{bi}$ up to $\varepsilon \approx 0.3$, in agreement with the $\varepsilon \ll 1$ prediction of [19].

The drift island theory employed here is valid for magnetic islands much smaller than the radius of the rational surface associated with them, i.e. $w \ll r_s$, and in the limit of low collisions away from the trapped-passing boundary. To allow the perturbative treatment of collisions, the particle collision frequency is assumed to be much smaller than the free streaming along the equilibrium magnetic field lines/characteristic drift frequency. The equilibrium radial electric field is set to zero. The contribution to the perturbed current density parallel to
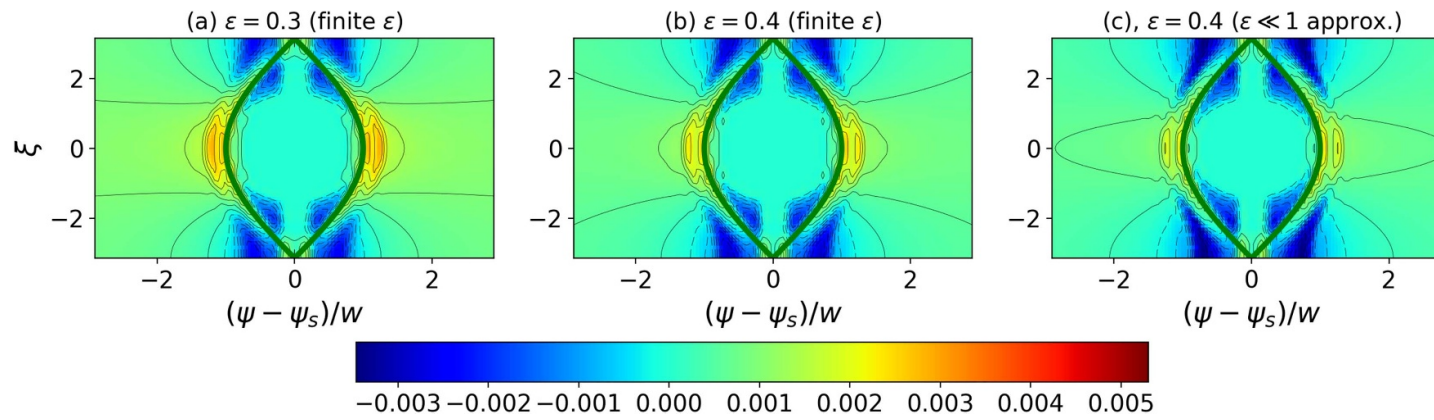
Figure 7. Colour contours showing the parallel current density, $j_\parallel$, in the (ψ, ξ) plane at $\rho_{\vartheta i}/w = 0.35$ at $\varepsilon = 0.3$ (*a*), $\varepsilon = 0.4$ (*b*) and $\varepsilon = 0.4$ (with the employed $\varepsilon \ll 1$ approximation) (*c*) in the absence of the parallel drift effects. $j_\parallel$ is normalised to $e n_0 V_{ti}$, where n_0 is the equilibrium density and V_{ti} is the ion thermal velocity. The parameters are $V = V_t$, $\kappa = 1.7$, $\delta = 0$, $\hat{L}_q = 1$ with the normalised equilibrium density and temperature gradient length scales $L_n/\psi_s = 1$, $L_T/\psi_s = 1$ for the m = 2, n = 1 mode. The green curve indicates the position of the magnetic island separatrix. Note, the small inverse aspect ratio approximation, invalid at finite ε, results in $\hat{L}_B^{-1} \propto \varepsilon$, enhancing negative flows around X-points at higher ε, e.g. see figures 7(*b*) and (*c*).
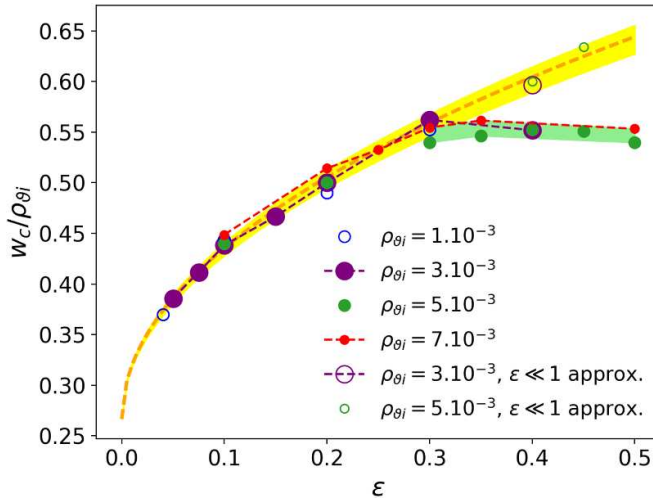
Figure 8. $w_c/\rho_{\vartheta i}$ plotted as a function of ε in the absence of the parallel drift effects. The parameters are $V = V_t$, $\delta = 0$, $\kappa = 1.7$, $\nu^* = 10^{-3}$, $\hat{L}_q = 1$ with the normalised equilibrium density and temperature gradient length scales $L_n/\psi_s = 1$, $L_T/\psi_s = 1$ for the m = 2, n = 1 mode. Note, $\rho_{\vartheta i}$ is in r_s units. The orange dashed line is the best fit line $\propto \varepsilon^{1/2}$ obtained in the small inverse aspect ratio tokamak limit [19].
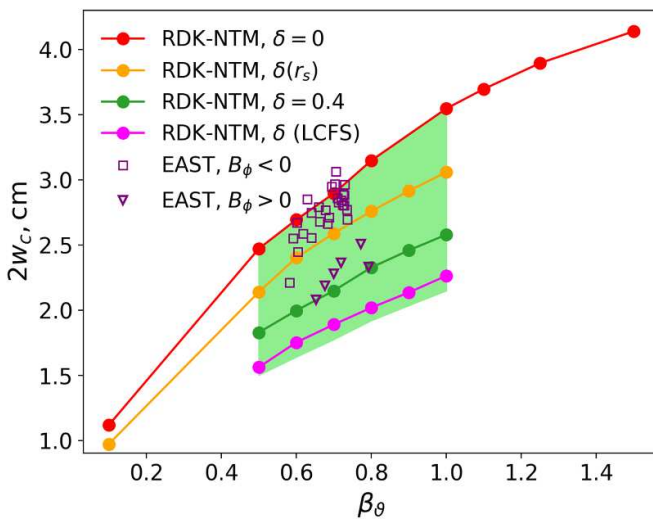
Figure 9. Threshold 2/1 magnetic island width plotted as a function of β_ϑ. Markers (square markers for $B_\varphi < 0$ and triangle markers for $B_\varphi > 0$) indicate the 2/1 NTM threshold for the 91972 EAST discharge [31]. $\varepsilon = 0.13$, $\kappa(r_s) = 1.25$, $\delta(r_s) = 0.13$, $s_\kappa = 0.07$, $s_\delta = 0.24$ at the 2/1 rational surface. $a/R_0 = 0.24$, $\delta = 0.53$ and $\kappa = 1.65$ at the last closed flux surface (LCFS). r_s indicates the position of the rational surface.

the field lines is then provided by a combination of bootstrap and curvature physics, as well as polarisation effects associated with the perturbed electrostatic potential.

As discussed in [16, 18, 19], the particle distribution function is found to be flattened across drift islands, shifted radially by a value proportional to the poloidal Larmor radius, compared to the magnetic island. This then supports a contribution to the density gradient associated with passing ions at $w \sim \rho_{\vartheta i}$. Since $\rho_{\vartheta e} \ll w$ ($\rho_{\vartheta e}$ is the electron poloidal Larmor

radius), the shift of the passing electron drift islands relative to the magnetic island is small, and therefore the electron density profile is still flattened across the magnetic island in the absence of the electrostatic potential. These differing responses generate a perturbed electrostatic potential to ensure plasma quasi-neutrality. The perturbed electrostatic potential together with the matching trapped-passing boundary layer [19] introduce the trapped particles into the dynamics. The $\varepsilon^{1/2}\rho_{\vartheta i}$ scaling of the threshold island width up to $\varepsilon \approx 0.3$ indicates this (see figure 8). At $\varepsilon > 0.3$, corrections associated with the finite aspect ratio cannot be neglected, and the expansion in powers of $\varepsilon \ll 1$ in the equilibrium magnetic field and its gradient length scale cannot be applied. $w_c \propto \varepsilon^{1/2}\rho_{\vartheta i}$ ($\sim \rho_{bi}$ in the limit of $\varepsilon \ll 1$) at $\varepsilon < 0.3$ is replaced with the $\rho_{\vartheta i}$ scaling of the threshold island width at $\varepsilon > 0.3$ in figure 8. Note, the fraction of trapped particles is

$$f_t = 1 - \frac{3}{4}\left\langle B_0^2 \right\rangle_\vartheta^\psi \int_0^{\lambda_c} \frac{\lambda d\lambda}{\left\langle \sqrt{1 - \lambda B_0} \right\rangle_\vartheta^\psi},$$

where $\langle \ldots \rangle_\vartheta^\psi$ denotes the orbit-averaging operator at fixed ψ. $f_t \sim \varepsilon^{1/2}$ in the limit of $\varepsilon \ll 1$ becomes $f_t \sim \varepsilon^{0.23}$ for finite aspect ratios. Therefore, $\rho_{bi} \sim \varepsilon^{1/2}\rho_{\vartheta i}$ for $\varepsilon \ll 1$ becomes $\rho_{bi} \sim (\Theta/\varepsilon^{0.23})\rho_{\vartheta i}$ for $\varepsilon \sim 1$. This suggests that the finite ε effects in equation 29 enhance the drift island contribution of passing particles in providing the threshold mechanism for NTMs.

6.3.4. Poloidal beta effects. In figure 9 we plot the 2/1 NTM threshold as a function of β_ϑ. As discussed above, β_ϑ enters the poloidal magnetic field component via $\partial_r R_0$. The ion poloidal Larmor radius is an input parameter in the RDK-NTM approach, and provides an additional $\propto \beta_\vartheta^{1/2}$ dependence on poloidal beta. This results in w_c being a growing function of β_ϑ at fixed ε and q. This dependence is in agreement with the recent EAST measurements of the critical island width (see figure 9) for the 2/1 NTM triggered by the resonant magnetic perturbations [31].

7. Conclusions and future work

We have extended the self-consistent drift island theory developed in [16–19] to a finite beta, arbitrary tokamak plasma configuration to capture the plasma shaping effects on the NTM threshold physics with a particular focus on non-zero plasma triangularity and finite aspect ratio. We focus on the neoclassical current perturbations localised in the vicinity of the rational surface, defining the threshold island half-width, w_c, as the value below which the neoclassical terms are stabilising. As these neoclassical drives exceed Δ' for islands of half-width w close to w_c, the association of w_c with the threshold is reasonable. Plasma shape parameters, including elongation and triangularity, are known to have a strong impact on tokamak plasma MHD stability. Triangularity is shown to influence the radial shift of passing particle drift islands relative to the magnetic island. This forms a theoretical basis for

the pressure gradient restoration across the magnetic island O-point at $w \sim \rho_{\vartheta i}$ and hence for the NTM threshold mechanism. Triangularity also influences the trapped particle bounce points and therefore has a direct impact on the trapped/passing particle orbits. We find that for magnetic islands of width $w \gtrsim \rho_{\vartheta i}$, positive triangularity enhances destabilising flows outside the island separatrix, while negative triangularity enhances stabilising flows around the separatrix in the vicinity of the X-points. For the equilibrium explored, the *threshold island width* is found to increase from $1.8\rho_{bi}$ at $\delta = 0.4$ (in agreement with experimental measurements) to $2.9\rho_{bi}$ at $\delta = -0.5$ ($\nu^* = 10^{-4}$) for the m/n = 2/1 NTM. As was shown in [19], the threshold also scales with the tokamak inverse aspect ratio as $\varepsilon^{1/2}$ in the limit of $\varepsilon \ll 1$. At $\varepsilon \gtrsim 0.3$, the $w_c \propto \varepsilon^{1/2}\rho_{\vartheta i}$ scaling of the threshold island width is replaced by $w_c \propto \rho_{\vartheta i}$. As was discussed in [19], the magnetic drift frequency and hence the NTM threshold prediction is sensitive to the gradient length scale of the confining magnetic field. The latter depends on the aspect ratio and plasma beta. The finite aspect ratio effects are found to enhance the stabilising flows around the island separatrix and (from the $w_c \propto \rho_{\vartheta i}$ scaling at $\varepsilon \gtrsim 0.3$) the contribution of drift islands associated with passing particles to the NTM threshold mechanism. Note, the equilibrium radial electric field is assumed to be zero in the island rest frame. The only polarisation contribution is then driven by a localised, perturbed electrostatic potential generated by the differing electron and ion responses. The role of this ion polarisation current in providing the threshold will be explored in our future publication.

While this work refines our previous threshold results, allowing the plasma shaping contribution in addition to the bootstrap current, the theory has certain limitations. One of them is related to the assumption that $B_\vartheta/B_0 \ll 1$ which is required to ensure $\delta_* \ll \Delta$ or $\rho_i \ll w \sim \rho_{bi} \sim \varepsilon^{1/2}\rho_{\vartheta i}$. While this is typically a good approximation for conventional tokamaks, including for non-circular, finite aspect ratio plasma equilibria, it might be invalid for certain spherical tokamak plasma equilibria. While we retain the $|\nabla_\perp| \sim 1/w$ (when acting on perturbed quantities related to the magnetic island perturbation) terms when calculating the plasma response to NTMs, certain effects associated with the sharp spatial variation, $|\nabla_\perp| \sim 1/\rho$, in perturbed quantities might be ordered out in the drift kinetic approach. To accurately include the $w \sim \rho$ effects and therefore to allow $B_\vartheta/B_0 \sim 1$, the drift kinetic theory has to be extended to the gyrokinetic limit which we will explore in future work. Extension to gyrokinetics to capture the finite Larmor radius effects might be relevant not only to certain spherical tokamak plasma equilibrium scenarios but also to the magnetic island separatrix boundary layer problem and therefore to the polarisation contribution to the threshold physics when an equilibrium electric field exists; it will also allow one to investigate the impact of the plasma turbulence on the layer physics.

In the present paper the dissipation processes are dominated by collisional dissipation in the vicinity of the trapped-passing boundary. This can be further extended to include other sources of dissipation, e.g. S diffusion in the separatrix boundary layer [19],[11] error fields/ coupling to a resistive wall (see e.g. [32, 33]). Furthermore, to make the theory applicable to a burning plasma of a reactor, one would need to include a population of fast particles produced by fusion reactions.

Acknowledgment

Data accessibility statement

The RDK-NTM numerical data is available at https://doi.org/10.5281/zenodo.6590135.

Disclaimer

Appendix A. Derivation of the extended drift kinetic equation

We expand equation (6) in powers of δ_*. The $\mathcal{O}\left(\delta_*^{-1}\frac{V_t}{L}f_0\right)$ equation then reads

$$\omega_c \left.\frac{\partial f_0}{\partial \alpha}\right|_{\boldsymbol{x},U,\mu} = 0, \qquad (A.1)$$

---

[11] This layer provides a significant contribution to current that is out-of-phase with the magnetic island, which determines how the magnetic island propagates through the plasma, and hence will likely influence the threshold prediction for rotating islands. This will be presented in future publications.

where we learn that the leading order distribution function, f_0, is independent of α at fixed $\boldsymbol{x}$. Proceeding to $\mathcal{O}\left(\delta_*^0 \frac{V_t}{L} f_0\right)$, we write

$$\omega_c \left.\frac{\partial f_1}{\partial \alpha}\right|_{\boldsymbol{x},U,\mu} + \mathcal{L}f_0 = Cf_0, \tag{A.2}$$

where $f_1 = \mathcal{O}\left(\delta_*^1 f_0\right)$. Averaging equation (A.2) over α at fixed $\boldsymbol{x}$ and applying equation (A.1), we obtain a drift kinetic equation to be solved for f_0:

$$\langle \mathcal{L} - C \rangle_\alpha^{\boldsymbol{x}} f_0 = 0. \tag{A.3}$$

Here $\langle \ldots \rangle_\alpha^{\boldsymbol{x}}$ represents $1/(2\pi) \oint \ldots d\alpha$ at fixed $\boldsymbol{x}$. Neglecting the difference between C and its gyro-averaged form, we reduce equation (A.3) to

$$\bar{\mathcal{L}}f_0 = Cf_0, \tag{A.4}$$

where $\bar{\mathcal{L}} \equiv \langle \mathcal{L} \rangle_\alpha^{\boldsymbol{x}}$ and is given by

$$\begin{aligned}
\bar{\mathcal{L}} = &\frac{\partial}{\partial t} + \boldsymbol{u} \cdot \boldsymbol{\nabla} - \frac{\mu}{B}\frac{\partial B}{\partial t} \left.\frac{\partial}{\partial \mu}\right|_{\boldsymbol{x},U,\alpha} \\
&+ \frac{eZ}{m}\left(\frac{\partial \Phi}{\partial t} - \boldsymbol{u} \cdot \frac{\partial \boldsymbol{A}}{\partial t}\right)\left.\frac{\partial}{\partial U}\right|_{\boldsymbol{x},\mu,\alpha}.
\end{aligned} \tag{A.5}$$

This form of the drift kinetic equation does not retain the plasma drift effects and thus we must capture the $\mathcal{O}\left(\delta_*^1 \frac{V_t}{L} f_0\right)$ corrections in addition to equation (A.2):

$$\omega_c \left.\frac{\partial (f_1 + f_2)}{\partial \alpha}\right|_{\boldsymbol{x},U,\mu} + \mathcal{L}(f_0 + f_1) = C(f_0 + f_1), \tag{A.6}$$

where $f_2 = \mathcal{O}\left(\delta_*^2 f_0\right)$. Gyro-averaging equation (A.6), we obtain

$$\bar{\mathcal{L}}f_0 + \langle \mathcal{L}f_1 \rangle_\alpha^{\boldsymbol{x}} = Cf_0 + C\langle f_1 \rangle_\alpha^{\boldsymbol{x}}. \tag{A.7}$$

To obtain f_1, we apply the recursive procedure discussed in [22] and combine equations (A.2) and (A.4) to write

$$\omega_c \left.\frac{\partial f_1}{\partial \alpha}\right|_{\boldsymbol{x},U,\mu} = (C - \mathcal{L})f_0 + \left(\bar{\mathcal{L}} - C\right)f_0,$$

which is equivalent to

$$\left.\frac{\partial f_1}{\partial \alpha}\right|_{\boldsymbol{x},U,\mu} = -\frac{1}{\omega_c}\tilde{\mathcal{L}}f_0, \tag{A.8}$$

where $\tilde{\mathcal{L}} = \mathcal{L} - \bar{\mathcal{L}}$. We note that this is valid only if the difference between C and its gyro-averaged form can be neglected[12]. Integrating equation (A.8), we obtain f_1 as a function of f_0:

$$f_1 = \boldsymbol{\rho} \cdot \boldsymbol{h}_1 + h_2 \tag{A.9}$$

---

[12] In the drift kinetic approach, the gyro-averaging is performed in the absence of the finite Larmor orbit width effects, i.e. is equivalent to averaging over α at fixed $\boldsymbol{x}$. For this case, the difference between C and $\langle C \rangle_\alpha^{\boldsymbol{x}}$ can be ignored. It can be demonstrated that for the like-species Fokker–Planck collision operator, $C = \langle C \rangle_\alpha^{\boldsymbol{x}}$ [22].

with

$$\boldsymbol{h}_1 = -\boldsymbol{\nabla}f_0 + \frac{eZ}{m}\left[\frac{\partial \boldsymbol{A}}{\partial t}\left.\frac{\partial f_0}{\partial U}\right|_{\boldsymbol{x},\mu,\alpha} - [\boldsymbol{b} \times \boldsymbol{V}_D]\left.\frac{\partial f_0}{\partial \mu}\right|_{\boldsymbol{x},U,\alpha}\right] \tag{A.10}$$

and

$$h_2 = \frac{u}{2B}\left\{[(\boldsymbol{s} \cdot \boldsymbol{\nabla})\boldsymbol{b}] \cdot \boldsymbol{\rho} - \frac{s^2}{2\omega_c}\frac{\mu_0 j_\parallel}{B}\right\}\left.\frac{\partial f_0}{\partial \mu}\right|_{\boldsymbol{x},U,\alpha}. \tag{A.11}$$

Here we chose $\langle f_1 \rangle_\alpha^{\boldsymbol{x}} = 0$ as a constraint to determine the constant of integration. Note,

$$\begin{aligned}
\boldsymbol{\nabla} \cdot \boldsymbol{b} &= -\boldsymbol{b} \cdot \boldsymbol{\nabla}\ln B = -[(\boldsymbol{e}_2 \cdot \boldsymbol{\nabla})\boldsymbol{e}_2 + (\boldsymbol{e}_3 \cdot \boldsymbol{\nabla})\boldsymbol{e}_3] \cdot \boldsymbol{b}, \\
\frac{\mu_0 j_\parallel}{B} &= [\boldsymbol{\nabla} \times \boldsymbol{b}] \cdot \boldsymbol{b} = [(\boldsymbol{e}_3 \cdot \boldsymbol{\nabla})\boldsymbol{e}_2 - (\boldsymbol{e}_2 \cdot \boldsymbol{\nabla})\boldsymbol{e}_3] \cdot \boldsymbol{b}.
\end{aligned} \tag{A.12}$$

Substituting equation (A.9) into equation (A.7), we obtain an extended drift kinetic equation for f_0 that captures the plasma drift effects, equation (12).

Appendix B. The $\left.\frac{d\mu}{dt}\right|_{\text{avg}}$ contribution

A straightforward expression for $\left.\frac{d\mu}{dt}\right|_{\text{avg}}$ that results from appendix A is

$$\begin{aligned}
\left.\frac{d\mu}{dt}\right|_{\text{avg}} = &-\frac{\mu}{B}\frac{\partial B}{\partial t} - \mu\{\boldsymbol{\nabla} \cdot \boldsymbol{V}_E + \boldsymbol{\nabla} \cdot \boldsymbol{V}_d \\
&+ (\boldsymbol{V}_E + \boldsymbol{V}_d) \cdot [\boldsymbol{\nabla}\ln B - (\boldsymbol{b} \cdot \boldsymbol{\nabla})\boldsymbol{b}]\} \\
&+ \frac{2\mu}{B}[\boldsymbol{b} \times (\boldsymbol{b} \cdot \boldsymbol{\nabla})\boldsymbol{b}] \cdot \frac{\partial \boldsymbol{A}}{\partial t}.
\end{aligned} \tag{B.1}$$

Substituting equation (15) into equation (B.1), one can show that

$$\begin{aligned}
&\boldsymbol{\nabla} \cdot \boldsymbol{V}_d + \boldsymbol{V}_d \cdot [\boldsymbol{\nabla}\ln B - (\boldsymbol{b} \cdot \boldsymbol{\nabla})\boldsymbol{b}] \\
&= -u\frac{\mu_0 j_\parallel}{B}(\boldsymbol{b} \cdot \boldsymbol{\nabla})\left(\frac{u}{\omega_c}\right) - 2\frac{u^2}{\omega_c}\frac{\mu_0}{B}(\boldsymbol{j}_\perp \cdot \boldsymbol{\nabla}\ln B),
\end{aligned}$$

$$\boldsymbol{\nabla} \cdot \boldsymbol{V}_E + \boldsymbol{V}_E \cdot [\boldsymbol{\nabla}\ln B - (\boldsymbol{b} \cdot \boldsymbol{\nabla})\boldsymbol{b}] = -\frac{1}{B}\frac{\partial B}{\partial t} - 2\boldsymbol{V}_E \cdot (\boldsymbol{b} \cdot \boldsymbol{\nabla})\boldsymbol{b}$$

and thus

$$\begin{aligned}
\frac{1}{\mu}\left.\frac{d\mu}{dt}\right|_{\text{avg}} = &u\frac{\mu_0 j_\parallel}{B}(\boldsymbol{b} \cdot \boldsymbol{\nabla})\left(\frac{u}{\omega_c}\right) + 2\frac{u^2}{\omega_c}\frac{\mu_0}{B}(\boldsymbol{j}_\perp \cdot \boldsymbol{\nabla}\ln B) \\
&+ \frac{2}{B}[\boldsymbol{b} \times (\boldsymbol{b} \cdot \boldsymbol{\nabla})\boldsymbol{b}] \cdot \left(\boldsymbol{E} + \frac{\partial \boldsymbol{A}}{\partial t}\right),
\end{aligned} \tag{B.2}$$

where $\boldsymbol{j}_\perp$ is the current density perpendicular to the magnetic field lines and can be expressed in terms of the plasma pressure gradient, provided plasma is in MHD equilibrium. To simplify equation (B.2) further, we cross equation (5) with $\boldsymbol{b}$ and average it over α at fixed $\boldsymbol{x}$. This provides

$$\frac{1}{\mu}\frac{d\mu}{dt}\bigg|_{\text{avg}} = u\frac{\mu_0 j_\parallel}{B}(\boldsymbol{b}\cdot\boldsymbol{\nabla})\left(\frac{u}{\omega_c}\right)$$
$$+ \frac{1}{\omega_c}\left(s^2 + 2u^2\right)\frac{\mu_0}{B}(\boldsymbol{j}_\perp\cdot\boldsymbol{\nabla}\ln B)$$
$$+ \frac{2}{B}[\boldsymbol{b}\times(\boldsymbol{b}\cdot\boldsymbol{\nabla})\boldsymbol{b}]\cdot\frac{\partial\boldsymbol{A}}{\partial t}$$
$$- \frac{2u}{\omega_c}\left[\boldsymbol{b}\times\frac{\partial\boldsymbol{b}}{\partial t}\right]\cdot(\boldsymbol{b}\cdot\boldsymbol{\nabla})\boldsymbol{b}. \qquad (\text{B.3})$$

equation (B.3) can be further reduced to equation (16), provided $\boldsymbol{\nabla}\cdot\boldsymbol{j} = 0$, where $\boldsymbol{j} = j_\parallel\boldsymbol{b} + \boldsymbol{j}_\perp$ is the total plasma current density.

ORCID iDs

A.V. Dudkovskaia ⓘ https://orcid.org/0000-0001-6890-3079

L. Bardoczi ⓘ https://orcid.org/0000-0002-8280-2423

J.W. Connor ⓘ https://orcid.org/0000-0001-9666-6103

D. Dickinson ⓘ https://orcid.org/0000-0002-0868-211X

P. Hill ⓘ https://orcid.org/0000-0003-3092-1858

K. Imada ⓘ https://orcid.org/0000-0002-8128-2438

S. Leigh ⓘ https://orcid.org/0000-0002-0376-9451

N. Richner ⓘ https://orcid.org/0000-0001-5544-3915

T. Shi ⓘ https://orcid.org/0000-0002-5321-1464

H.R. Wilson ⓘ https://orcid.org/0000-0003-3333-7470

References

[1] Hender T.C. *et al* 2007 Progression in the ITER Physics Basis. Chapter 3: MHD stability, operational limits and disruptions *Nucl. Fusion* **47** S128–202

[2] Qu W.X. and Callen J.D. 1985 University of Wisconsin report UWPR 85-5

[3] Carrera R., Hazeltine R.D. and Kotschenreuther M. 1986 *Phys. Fluids* **29** 899

[4] Poli E. *et al* 2015 *Nucl. Fusion* **55** 013023

[5] Rutherford P.H. 1973 *Phys. Fluids* **16** 1903–8

[6] Sauter O. *et al* 1997 *Phys. Plasmas* **4** 1654

[7] Sauter O., Buttery R.J. and Felton R., Hender T.C., Howell D.F. and contributors to the EFDA-JET Workprogramme 2002 *Plasma Phys. Control. Fusion* **44** 1999–2019

[8] Buttery R.J. *et al* 2000 *Plasma Phys. Control. Fusion* **42** B61–B73

[9] Wilson H.R., Connor J.W., Hastie R.J. and Hegna C.C. 1996 *Phys. Plasmas* **3** 248

[10] Fitzpatrick R. 1995 *Phys. Plasmas* **2** 825

[11] Hazeltine R.D., Helander P. and Catto P.J. 1997 *Phys. Plasmas* **4** 2920

[12] Poli E., Peeters A.G. and Bergmann A. 2002 *Phys. Rev. Lett.* **88** 075001

[13] Poli E., Peeters A.G. and Bergmann A. *et al* 2003 *Plasma Phys. Control. Fusion* **45** 71–87

[14] Poli E., Bottino A., Hornsby W.A., Peeters A.G., Ribeiro T., Scott B.D. and Siccinio M. 2010 *Plasma Phys. Control. Fusion* **52** 124021

[15] Poli E., Bergmann A. and Casson F.J. *et al* 2016 *Plasma Phys. Rep.* **42** 450–64

[16] Imada K., Wilson H.R., Connor J.W., Dudkovskaia A.V. and Hill P. 2018 *Phys. Rev. Lett.* **121** 175001

[17] Imada K., Wilson H.R., Connor J.W., Dudkovskaia A.V. and Hill P. 2018 *J. Phys. Conf. Ser.* **1125** 012013

[18] Imada K., Wilson H.R., Connor J.W., Dudkovskaia A.V. and Hill P. 2019 *Nucl. Fusion* **59** 046016

[19] Dudkovskaia A.V., Connor J.W., Dickinson D., Hill P., Imada K., Leigh S. and Wilson H.R. 2021 *Plasma Phys. Control. Fusion* **63** 054001

[20] Kotschenreuther M., Hazeltine R.D. and Morrison P.J. 1985 *Phys. Fluids* **28** 294

[21] Lutjens H., Luciani J.-F. and Garbet X. 2001 *Phys. Plasmas* **8** 4267

[22] Hazeltine R.D. and Meiss J.D. 1992 *Plasma Confinement* (New York: Addison-Wesley) p 125

[23] La Haye R.J., Prater R., Buttery R.J., Hayashi N., Isayama A., Maraschek M.E., Urso L. and Zohm H. 2006 *Nucl. Fusion* **46** 451–61

[24] La Haye R.J., Buttery R.J. and Gerhardt S.P., Sabbagh S.A. and Brennan D.P. 2012 *Phys. Plasmas* **19** 062506

[25] Miller R.L., Chu M.S., Greene J.M., Lin-Liu Y.R. and Waltz R.E. 1998 *Phys. Plasmas* **5** 973

[26] Todd A.M.M., Manickam J., Okabayashi M., Chance M.S., Grimm R.C., Greene J.M. and Johnson J.L. 1979 *Nucl. Fusion* **19** 743

[27] Lao L.L., Hirshman S.P. and Wieland R.M. 1981 *Phys. Fluids* **24** 1431

[28] Faugeras B. 2020 *Fusion Eng. Des.* **160** 112020

[29] Crotinger J.A., LoDestro L., Pearlstein L.D., Tarditi A., Casper T.A. and Hooper E.B. 1997 *Corsica: A Comprehensive Simulation of Toroidal Magnetic-Fusion Devices Final Report to the LDRD Program UCRL-ID-126284*

[30] Wilson H.R., Connor J.W., Dickinson D., Dudkovskaia A.V., Hill P., Imada K. and Leigh S. 2021 Drift-kinetic theory of neoclassical tearing modes close to the threshold in tokamak plasmas *28th IAEA Fusion Energy Conf.*

[31] Shi T. *et al* (arXiv:2103.15506) [physics.plasm-ph]

[32] Smolyakov A.I., Hirose A., Lazzaro E., Re G.B. and Callen J.D. 1995 *Phys. Plasmas* **5** 1581

[33] McAdams R., Wilson H.R. and Chapman I.T. 2013 *Nucl. Fusion* **53** 083005